

# Rotor Inflow Noise Caused by a Boundary Layer: Inflow Measurements and Noise Predictions

Michael Morton<sup>1</sup>, William Devenport<sup>2</sup>, W. Nathan Alexander<sup>3</sup>  
*Virginia Tech, Blacksburg VA 24061*

Stewart A. L. Glegg<sup>4</sup>  
*Florida Atlantic University, Boca Raton FL 33431*

Aurelien Borgoltz<sup>5</sup>  
*Virginia Tech, Blacksburg VA 24061*

Detailed measurements of the four-dimensional space time correlation function of a thick turbulent boundary layer have been made and used as source terms for the prediction of sound radiated from a 10-bladed rotor partially immersed in this flow. This simple configuration recreates in a canonical setting the important physics produced when a rotor ingests inhomogeneous anisotropic turbulence, without many of the complications present in most practical applications. The correlation measurements show substantial turbulence anisotropy in the body of the boundary layer which is characterized by streamwise elongated structures inclined relative to the wall. Translated to the rotor frame this anisotropy leads substantial asymmetry in blade-to-blade upwash coherence. Predictions of radiated sound spectra and directivity are performed for a range of conditions. Sound predictions reveal spectra dominated by ‘haystacking’ - distinct peaks at multiples of the blade passing frequency produced by multiple cutting of the same turbulent structures.

## I. Introduction

Rotating blade systems operating in a fully turbulent non-uniform flow generate noise from the fluctuating loads on the blade surfaces. An important example of this is the embedded aircraft engine. Engine embedding is seen in military aircraft as a way to minimize vehicle signature, and has been considered for civil transport applications as a way to improve efficiency and reduce noise (such as with the SILENT aircraft initiative, Hileman et al., 2007, or the Blended Wing Body concept, Ko et al., 2003). Such designs usually involve mounting the engine intakes towards the trailing edge of the wing with the intent of improving the cruise fuel burn by drawing in the thickest parts of the suction-side boundary layer (Plas et al., 2007). A side effect of this is a thick turbulent rotational flow entering the fan face at all phases of the aircraft operation and the resultant noise and vibration it produces. Accommodating this remains a significant challenge (de la Rosa Blanco, 2007). This application has important complexities such as a non-uniform shear flow entering the engine, stretching of the incoming turbulence, and interaction of that turbulence with the fan.

Early efforts on turbulence ingestion include the work of Sevik (1970) at Penn State. He looked at the unsteady thrust on a 10-bladed propeller mounted in a water tunnel downstream of turbulence generating grids. This arrangement was modeled by assuming that the ingested turbulence was homogeneous and isotropic and governed by an exponentially decaying correlation function. The general trend of the predictions and measurements matched quite well, with the exception that the spectrum contained ‘humps’ or ‘haystacks’ at multiples of the blade rate. The

<sup>1</sup> Graduate Research Assistant, Department of Aerospace and Ocean Engineering, AIAA Student Member.

<sup>2</sup> Professor, Department of Aerospace and Ocean Engineering, AIAA Associate Fellow.

<sup>3</sup> Postdoctoral Research Associate, Department of Aerospace and Ocean Engineering, AIAA Member.

<sup>4</sup> Professor, Department of Ocean and Mechanical Engineering, AIAA Associate Fellow.

<sup>5</sup> Research Scientist, Department of Aerospace and Ocean Engineering, AIAA Member.

reason for this mismatch was that Sevik did not consider that some turbulence structures might be cut by more than one blade so that the fluctuating loads from blade to blade would be correlated to some extent. This effect was subsequently incorporated into analysis of the problem by Blake (1986), Martinez (1997), Glegg and Walker (1998), Joseph and Parry (2001) and Atassi and Logue (2009), among others.

There are two factors that contribute to blade-to-blade correlation. The first is simply the advance ratio of the rotor. If this is sufficiently small then successive blades will cut closely-spaced spiral paths through the fluid material, and thus meet the same turbulence. If the blade count is high then the non-dimensional time delay between these cuts will be small, further increasing the correlation. The second is the distortion of turbulence as it is drawn into the rotor. The flow accelerates towards the rotor plane and this tends to orient and stretch the turbulence structures in the streamwise direction, increasing the opportunity for multiple cuts by successive blades.

The most extreme example of distortion is the ingestion of atmospheric turbulence into stationary aircraft engines, as first studied by Hanson (1974). He examined the turbulence drawn into the inlet using hot-wire anemometry, and the resulting response of the blades with pressure transducers embedded within them. In this case the substantial contraction of the flow entering the engine inlet was found to produce turbulence scales with a 400:1 streamwise to cross stream aspect ratio and a length on the order of 100 fan diameters. These inlet vortices produced short distinct lift pulses as they were cut multiple times by the rotating blades. This specific situation was analyzed by Majumder and Peake (1998) using rapid distortion theory, assuming initially isotropic turbulence and computing the sound radiated by the fan using strip theory. In cruising flight the stretching of turbulence approaching the fan is considerably less than for a stationary engine but, as noted by Majumder and Peake, this is still an important effect. In the specific case of an embedded aircraft engine, the installation is specifically designed to draw in the suction side boundary layer and thus, one anticipates that stretching will be an important factor.

Ingestion of rather less distorted homogeneous turbulence into a rotor has been the subject of a series of studies in the anechoic wind tunnel at the University of Notre Dame, including work by Sharpf and Mueller (1995), Minniti *et al.* (2001, 2001a), Wojno *et al.* (2002, 2002a) and Lynch *et al.* (2005, 2005a, 2005b). Sharpf and Mueller studied the interaction of turbulence from three different grids with a 10-inch diameter, four-bladed, rotor. The grid turbulence was measured using hot-wire anemometry 0.6 diameters upstream of the rotor and found to be largely undistorted and of quite small scale (0.34 to 0.44 inches). Broadband sound levels radiated by the rotor were found to increase by 2dB for every 1% increase in turbulence level. Spectral humps associated with blade to blade correlations were only observed when the turbulence grid was removed and the larger (3-4 inch) eddies associated with facility background turbulence were ingested. Wojno *et al.* used similar turbulence generating grids but with the 10-bladed rotor of Sevik's earlier experiment. The cross sectional structure of the undisturbed turbulence, including the lingering imprint of the turbulence grid bars, was measured in detail. Measurements were not made in the rotating frame but measured velocity spectra were converted to the rotating reference frame assuming Taylor's hypothesis and relying on the homogeneity of the turbulence. Predictions of the broadband sound radiated by the rotor made using strip theory and the summation gain approach of Blake (1986), which accounts for the blade to blade correlation. Predictions showed good agreement with sound measurements, but with some differences that suggested an unaccounted for additional broadband source. Differences in the narrowband features of the spectrum also suggested that the blade to blade correlation was being underestimated. Minniti *et al.* studied a four-bladed propeller instrumented with PVDF pressure sensors mounted to the blades in order to measure pressure fluctuations and their spanwise correlation. By idealizing the blade response function they were able to infer the characteristics of the rotor inflow from the surface pressure fluctuations, an idea previously discussed theoretically by Grace *et al.* (1996, 1996a). Tests were done with cyclic inflow distortions, to calibrate the response function of the blades, and then with grid turbulence. Inflow turbulence predictions made using the pressure response agreed well with hot-wire measurements made in the rotating frame. This was done by mounting a hot wire probe on one of the blades with the sensor just forward of its leading edge. Far-field sound predicted from the inflow turbulence also agreed well with direct measurements. Lynch *et al.* (2005, 2005a, 2005b) focused on the response of an airfoil placed downstream of a rotor that was ingesting turbulence. They developed an empirical model of the turbulence wavenumber spectrum by assuming equal energy in all directions but with non-isotropic scales. This is done by manipulating the relationships between spectra and correlations of different components that exist in isotropic turbulence. Turbulence and mean flow measurements were made downstream of the rotor and analyzed to separate the contributions from the blade wakes and the ingested turbulence. The latter showed suppression of blade normal velocity fluctuations, consistent with the rapid distortion theory predictions of Graham (1998).

Studies of boundary layers being drawn into rotors have largely focused on the axisymmetric casing and hub boundary layer flows, as opposed to the thick plane boundary layer of an airplane wing. In conventional aircraft applications inlet boundary layers tend to be thin. Particularly well known here are the experiments of Ganz *et al.* (1998) on the Boeing 18-inch fan, a high-bypass-ratio fan model with an extended inlet duct. By running the fan

with and without suction to remove the 1cm thick inlet boundary layer Ganz *et al.* were able to show that the fan tip/boundary layer interaction was a significant noise source, and one that produced spectra humps indicative of blade to blade correlation. This specific experiment was later modeled by Glegg and Walker (1999) using a von Karman turbulence spectrum modified to account for the axial stretching of the turbulence in the approach to the fan face. Joseph and Parry (2001) also modeled this experiment, but using an empirical boundary layer turbulence spectrum based on earlier work by Gavin and Lauchle (2000). In both these theoretical studies the ratio of streamwise to spanwise scales in the boundary layer had to be substantially exaggerated over that measured in the experiment in order to replicate the oscillating form of the measured sound spectrum.

A detailed experimental study of casing-boundary layer/rotor interaction has more recently been completed by Stephens and Morris (2009). Here the 10-bladed rotor of Sevik was mounted in a 206-mm diameter circular duct. Air was drawn through the duct independently of the rotor speed allowing for variations in the flow coefficient. The rotor was placed at different distances downstream from the duct entrance to vary the thickness of the boundary layer interacting with the blade tips. Close to the duct entrance the boundary layer was thin enough for its noise contribution to be small and for the self-noise of the rotor to be separately identified, and then subtracted from measurements. Boundary layer interaction noise was studied with the rotor 1.2 diameters downstream of the entrance, where the boundary layer thickness was 11mm, with the fan almost unloaded. Perpendicular-to-wall space time correlations of the streamwise velocity component were measured in the boundary layer, and then extrapolated into a model of the full 4-D boundary layer correlation function by assuming an exponential decay model. As discussed by Devenport *et al.* (1998) the 4D correlation is sufficient in principle to estimate the space time structure of the turbulence seen by a blade cutting the turbulence in any frame of reference. As such Stephens and Morris were able to use the measured turbulence properties and strip theory to determine the unsteady blade loading and thus the radiated sound, which was found to agree remarkably well with direct measurements. With an axisymmetric bump installed in the duct to increase the boundary layer thickness by a factor of 2.8, and with semi-empirical scaling of the correlation function, similarly good agreement was achieved.

The literature includes a number of studies involving hub boundary layer ingestion. Moiseev *et al.* (1978) considered a 10 and 17-bladed shrouded compressor rotors installed in a long annular inlet duct. The inlet was long enough that turbulent flow associated with the hub and casing boundary layers completely filled the cross section at the rotor inflow. Measurements were performed with and without an inlet turbulence grid and with the hub boundary layer modified by adding a heavy trip or by removing the hub nose cone and adding roughness. Turbulence measurements, including circumferential correlations, were measured upstream of the fan face. Sound measurements were made in the anechoic chamber containing the inlet. The grid greatly reduced turbulence integral scales, but in all cases considerable anisotropy was observed, with axial scales an order of magnitude larger than circumferential scales. Overall sound levels were found to correlate with the product of the mean-square turbulent fluctuation and the lengthscale.

Muench (2001) considered the sound radiated by a 6-bladed open propeller operating downstream of a stator row at the downstream end of an axisymmetric body. The primary focus of this study was on the mean flow downstream of the stators, and its interaction with the rotating propeller to generate tone noise, rather than on the distortion and ingestion of the turbulence structure. Muench was able to make an impressive array of phase locked measurements in the rotating frame, including detailed cross sections of the flow between the stator and rotor (made using hot-wire probes traversed from the rotating portion of the hub) and PVDF pressure sensors mounted on the blade surfaces. These measurements were made possible by a liquid mercury slip ring system. Huyer and Snarski (2003) continued the study of this configuration with turbulence and spectral measurements in the rotating frame. These showed the relatively thick hub boundary layer (extending out to about 80% of the rotor radius) to have a quite full turbulence profile with a broad region of elevated turbulence levels near the wall. This suggests that deceleration of the flow over the upstream axisymmetric body was more important in distorting the boundary layer structure than the acceleration of the flow into the rotor. Integral scales were found to be about 5% of the rotor radius. Huyer and Beal (2007) used these measurements in an attempt to predict radiated noise from the rotor. A lifting surface propulsor code was used with the inflow modulated so as to match the hot-wire measured spectra, with random phase. Spanwise correlations were simulated by controlling relative phase angle in this direction. Predictions of the overall broadband noise level were in overall agreement with measurements.

An important component of a thick inlet boundary layer is its mean flow shear. Shear substantially complicates the analysis of the turbulence distortion problem, and the estimation of blade response, not least because it complicates the rapid distortion theory that forms the basis of many theoretical models of ingestion. While not explicitly studied, the effects of circumferentially uniform shear presumably impacted the results of the above experimental studies of hub boundary layer ingestion. Radially aligned shear is also implicit in the cyclic inflow distortions studied by Subramanian and Mueller (1995) and Minniti *et al.* (2001, 2001a), and the radial obstructions

studied by Mugridge (1975) and Kota and Wright (2006) although none of these authors considered the effects of the shear upon the turbulence and its distortion approaching the rotor face.

While there has been much work on turbulence ingestion and on the blade response and the sound that it generates, there have been no previous studies that directly address the problem of a rotor ingesting turbulence from a plane boundary layer with a thickness comparable to the rotor radius. As detailed above this is a complex problem for which the major unknowns are the distortion of the shear-flow boundary layer turbulence entering the rotor plane and the resulting response of the rotor. In essence we don't know most of the details of the turbulence actually seen by the rotor blades and how it is related to the upstream flow and the sound radiated.

In most practical applications the non-uniform turbulent flow impacting on the rotor contains many complexities that are specific to the configuration and mask the important physical processes involved. Our approach in this experimental study is to examine a greatly simplified configuration that retains the fundamental physics but minimizes confounding factors. Our plan is to study in depth the aerodynamics and acoustics of a simple straight-bladed rotor partially immersed in a canonical two dimensional high Reynolds number boundary layer. The first phase of this study is to document space time correlation measurements of the turbulent boundary layer so that complete aeroacoustic inflow boundary conditions are known. The second phase involves the installation of the rotor, the measurement in the rotating frame of the turbulent inflow actually seen by the blades, and the comparison of that with the undisturbed boundary layer and predictions of the distortion of the flow as it is drawn into the fan. The final phase is to include measurements of the radiated sound.

In this paper we present the results of the first phase. A 100-mm thick plane two-dimensional boundary layer has been generated with mean velocity and turbulence stress profiles that closely match expectations for this type of flow. Using two 3-component hot-wire probes under computer control, and measurement grids designed using a DNS simulation data base, over 1,700 nine-component velocity cross-spectra have been measured in this flow in such a manner as to completely define the 4-dimensional space time correlation function of the turbulence at the location where the rotor will be installed. This database can be interrogated to reveal the spanwise and timewise correlation of the turbulence that would be encountered along the leading edge of any blade or set of blades cutting the turbulence on any path. In this paper we present this data and analyze the correlations, and thus broadband and tone noise sources, that would be encountered by the 10-bladed Sevik rotor. We find, among other things, that such a rotor will produce a sound spectrum dominated by the haystacking phenomenon.

## II. Experimental Setup

### A. Wind Tunnel and Test Wall

All data presented were taken in the the Stability Wind Tunnel at Virginia Tech as it is particularly well suited to velocity and sound measurements at high Reynolds number. The free stream flow through the  $1.83 \times 1.83 \times 7.3$  m long test section is closely uniform and has a very low turbulence level (0.01% to 0.03%). Flow speeds can be varied from 10 to 80m/s. The tunnel is unique in having interchangeable test section systems suited to aerodynamic and aeroacoustic measurements. The aeroacoustic test section system, shown in figures 1 and 2, was used in all the present work.

The unmodified system consists of an acoustic test section flanked by two anechoic chambers, as seen in Figure 1. The floor and ceiling of the test section are formed by porous walls backed by acoustic foam wedges designed to suppress any acoustic reflections. The side walls of the test section are dominated by 'acoustic windows' – tensioned panels of thin and light Kevlar 120 cloth that extend over the full height of the test section and 4.2 m of its streamwise length. The cloth is almost transparent to sound and thus sound associated with the flow in the test section can escape almost unhindered into the two anechoic chambers that cover the outside of these panels. This arrangement greatly reduces the level of parasitic noise in the test section, and enables the measurement of flow-generated sound using microphones placed outside the flow in the anechoic chambers. The containment of the flow by the Kevlar wall also eliminates the need for a jet catcher and minimizes aerodynamic interference corrections. Further details of the facility and its anechoic system are given by Devenport *et al.* (2010).

For the present work the anechoic test section was modified so as to produce a semi-anechoic arrangement. The starboard side acoustic window was removed and a hard wall installed extending along the entire length and height of the test section, Figure 2. The wall was mounted inside the original location of the acoustic window, reducing the test section width by 0.12-m. A curved fairing was used to smoothly connect the forward end of the wall to the curved wall of the contraction. This wall was used to grow the equilibrium turbulent boundary layer used for rotor inflow studies.

The wall is fabricated from six 1.22-m long Lexan panels supported from outside the flow by aluminum bean structure. The structure allows the panels to be aligned with each other, so as to avoid any steps at the panel joints,

and also adjusted to control the exact test section width at any streamwise position. This adjustment is used to zero out any residual streamwise pressure gradient. Trips placed on the contraction fairing, 1.2-m upstream of the forward edge of the false wall, are used to initiate spanwise uniform boundary layer growth.

Properties of the boundary layers produced using several different trips placed at the upstream end of the false wall in the facility contraction are reported by Forest and Devenport (2010) and are analyzed independently in this study for consistency. These measurements show the boundary layers to be closely two-dimensional and have properties consistent with the results of previous high Reynolds number boundary layer studies. With several candidate boundary layers available, this study chose to focus on a boundary layer generated by a 9.5-mm high two-dimensional fence trip for a free-stream velocity of 30 m/s. The properties of this boundary layer are discussed in detail below.

## B. Turbulence Measurement

Measurements of the mean and turbulent velocities in the boundary layer were accomplished using four-sensor hotwire anemometer probes shown in Figure 3. Sensors are arranged as two orthogonal X-wire arrays with each sensor inclined a nominal  $45^\circ$  from the probe axis. The four sensors are etched tungsten wire  $5\text{ }\mu\text{m}$  in diameter and approximately 1.2 mm in length equating to a nominal measurement volume of  $0.75\text{ mm}^3$ . The 4<sup>th</sup> sensor provides a measure of redundancy in obtaining the instantaneous components of velocity that can be used to extend the acceptance cone of the probe, or minimize susceptibility to certain gradient errors. Probes were operated using Dantec Streamline anemometers, the outputs of which were recorded using an Agilent E1432 16-bit digitizer controlled using Agilent Vee programs developed in-house. Probes were calibrated directly for a three-dimensional flow angle using the look-up table method of Wittmer *et al.* (1998) and for velocity based on King's law. The measurements were made at a distance of 4.72 meters downstream of the trip, a location comparable to previous experiments.

In order to measure two-point correlations in the flow, two separate traverse systems were installed as seen in Figure 3. A traverse capable of travelling in three dimensions was mounted inside the test section and another traverse capable of travelling in one dimension was mounted through the false wall. Both traverse systems were operated by a laptop computer and controllable down to movements of 0.025 mm. Mounted to the single axis traverse is a 0.41 meter long 9.5mm diameter rod that travels through the Lexan wall and into the test section. The three axis traverse consisted of two streamwise rails that mount to the ceiling panels of the test section, another two that mount to the floor panels, and two vertical rails. A horizontal rail connects the two vertical rails and is used to mount measurement instrumentation. Mounted on the horizontal rail are two 1.0 meter beams that extend forward of the traverse gear in the streamwise direction and hold a 0.46 meter long rod that extends toward the wall for probe mounting. A damping device was connected to one of the 1.0 meter support beams to reduce any vertical vibrations that might occur. Fully installed, the traverse systems created approximately an 11% blockage in the test section. The quad-wire probes were positioned using a Micro-Epsilon optoNCDT-1300-50 laser displacement sensor, operated through the Lexan test wall.

In order to achieve a minimum probe separation of 4 mm in both the streamwise and normal-to-wall directions, each probe needed to be pitched and yawed. Probe angles were determined using a laser pointer inserted into a rapid prototyped plastic part that fit directly into the probe holders. The laser was directed onto a sheet of grid paper that was aligned with the axes of the test section and taped to the wall. By moving the three axis traverse a known distance in the normal-to-wall direction and recording the laser's initial and final locations on the grid paper the pitch and yaw angles could be calculated. In this experiment positive pitch corresponded to the positive y direction and positive yaw to the positive z direction. The probe mounted on the single axis traverse remained at a yaw angle of  $-5.67$  degrees and a pitch angle of  $4.00$  degrees throughout all measurements. The probe on the three axis traverse varied between yaw angles of  $-13.35$  and  $-13.82$  degrees and pitch angles of  $-2.76$  and  $-5.11$  degrees. Visually inspecting the probes during testing showed that each probe occasionally vibrated in the y-direction a distance of no more than one prong diameter (0.1 mm).

Two-point measurement grids were designed using space time correlation estimates based on channel flow simulations by Moser *et al.* (1999) and adaptive traversing techniques developed to minimize the necessary measurement time. Although Moser's direct numerical simulation is for channel flow, it is reasonable to expect sufficient similarity in the boundary layer along the false wall in the Stability Wind Tunnel. Using the correlation function from Moser, a three dimensional grid was designed to get a high resolution of points where the correlation was largest. This three dimensional grid consisted of 31 fixed probe locations each of which included the moving probe measuring a cross section of 31 points in z (normal to wall) and 14 in y (spanwise) totaling 13,454 points. The grid was then divided into 31 subsets each of which corresponded to a unique fixed probe location. To simplify the traversing and reduce the possibility of a collision between the probes, the grids were modified so the moving probe

would never need to travel closer to the wall than the fixed probe. Additionally points were removed from all the grids to eliminate unnecessarily fine special resolution at large separations. A further factor of two reduction in the number of grid points was made using the expected symmetry properties of the boundary layer in the spanwise direction. These measures reduced the total measurement task to the measurement of 31 grids at 31 fixed probe locations totaling 1,781 points.

To further reduce the necessary measurement time adaptive traversing techniques were used. This was done by having the two-point measurement code monitor the coherence between velocity signals from the two probes and decide when measurements at greater separation were no longer relevant. Since determining the full two-point space time correlation was the principal objective of this study, all 31 grids were measured continuously spanning a total of 18 hours. This ensured that all velocity calibrations were similar and probe positioning was consistent for each grid.

After applying the appropriate probe angle rotations to the data, issues appeared in the Reynolds stress measurements made with probe yaw angle greater than 8 degrees. Comparisons between fixed probe (low yaw) and moving probe (high yaw) results showed discrepancies in the Reynolds shear stresses as large as 20%. This error was believed to originate in inaccuracies in local slope of the angle calibration at large angles. It was corrected, in both the single and two point results, by using the comparison of the erroneous moving probe stress measurements with the correct values from the fixed probe to infer the calibration slope error matrix. If the corrected moving probe fluctuating velocity components are denoted as  $u'_T$ ,  $v'_T$ ,  $w'_T$  and the measured fluctuating velocity components are denoted as  $u'$ ,  $v'$ ,  $w'$ , then the slope correction matrix  $\mathbf{T}$  relates these components as

$$\begin{Bmatrix} u'_T \\ v'_T \\ w'_T \end{Bmatrix} = \begin{bmatrix} T_{11} & T_{12} & T_{13} \\ T_{21} & T_{22} & T_{23} \\ T_{31} & T_{32} & T_{33} \end{bmatrix} \begin{Bmatrix} u' \\ v' \\ w' \end{Bmatrix} \quad (1)$$

The matrix  $\mathbf{T}$  can be determined by minimizing the difference between the fixed probe and moving probe stress profiles as previously performed by Borgoltz (2007). The resulting  $\mathbf{T}$  matrix for the moving probe at a yaw angle of 13.8 degrees is shown below in equation 2. This matrix is within a few percent of the identity matrix implying only small corrections to the calibration surface slope were needed.

$$\mathbf{T} = \begin{bmatrix} 0.9816 & 0.0099 & -0.0483 \\ -0.0139 & 1.0299 & 0.0306 \\ -0.019 & 0.0131 & 1.0562 \end{bmatrix} \quad (2)$$

### III. Flow Measurements

Measurements are presented using the coordinate system shown in Figure 2(a). Coordinate  $x$  is measured in the streamwise direction from the location of the trip, spanwise position  $y$  is measured from the mid-span of the tunnel, and normal to wall distance  $z$  is measured in the wall-normal direction. Velocity components  $u$ ,  $v$ , and  $w$  are defined in the  $x$ ,  $y$  and  $z$  directions respectively.

Mean pressures measured along the test section walls were used to monitor the streamwise pressure gradient imposed on the growing boundary layer. Pressure coefficient varied less than  $\pm 0.01$  in the test section upstream of  $x = 5\text{m}$  (see Forest and Devenport, 2011). All velocity and turbulence measurements were made at  $x = 4.72\text{m}$ , this being the location at which the model rotor is to be installed. Cross-sections in the  $y$ - $z$  plane were used to verify spanwise uniformity and the two dimensionality of the flow at this station. All the two-point turbulence measurements were made for a free stream velocity of 30m/s. Single point velocity and turbulence measurements were also made at other speeds to provide justification for scaling two-point correlation measurements to other flow velocities. Velocities are normalized on the free stream velocity  $U_{ref}$  sensed using a Pitot static tube located at  $(x, y, z) = (4.43\text{m}, -0.59\text{m}, 1.25\text{m})$ .

#### A. Mean velocity, Reynolds Stresses

Mean velocity and Reynolds stress profiles for free stream velocities of 30 and 20m/s are shown in figure 4. At both speeds the mean streamwise velocity profiles (Figure 4(a)) indicate a boundary layer thickness of close to 101mm and have a form that is fairly typical of a fully developed zero pressure gradient two-dimensional turbulent boundary layer. Plotted in inner variables (Figure 4(c)) the profiles show a semi-logarithmic region that compares well to a standard law of the wall profile using a von Karman constant of 0.41 and an offset of 5.2. Skin friction coefficients of 0.00258 (30m/s) and 0.00275 (20m/s) were estimated by comparison with this profile. By using the law of the wall to extend the measured profiles to the wall integral thicknesses and Reynolds numbers could be

estimated. The displacement and momentum thicknesses, and momentum thickness Reynolds numbers, were found to be 11.6 mm, 9.2mm and 16,600 at 30m/s and 12 mm, 9.4 mm and 11,500 at 20m/s. Note that the boundary layer profiles and parameters at 30m/s are quite consistent with values reported by Awasthi *et al.* (2011) based on single hot-wire measurements.

Shown in Figure 4(b) are the three turbulent normal stresses and the non-zero Reynolds shear stress  $uw$ . As would be expected  $u^2$  is the largest of the three normal stresses and rises monotonically as the wall is approached (the finite size of the 4-sensor probe did not allow measurements close enough to the wall to reveal the maximum in this profile). Spanwise velocity fluctuations  $v^2$  are about half of  $u^2$ , and normal to wall fluctuations  $w^2$  slightly less than that, particularly close to the wall where normal fluctuations are suppressed by the non-penetration condition. The negative Reynolds shear stress does reach a clear maximum in the bottom 20 % of the boundary layer thickness. The maximum values of  $1.2$  to  $1.3 \times 10^{-3}$  appear consistent with the boundary layer skin friction coefficients inferred from the mean velocity profiles. Normalized on the free stream velocity, the turbulence stress profiles are almost identical at the two speeds with the exception of slightly larger values if  $u^2$  and  $uw$  at 20m/s. This suggests that scaling the turbulence properties on the free stream velocity should be sufficient when estimating acoustic source terms for this range of speeds.

Figure 5 shows autospectra of velocity fluctuations measured at representative points throughout the boundary layer. At the boundary layer edge ( $z/\delta=101\%$ ), the  $u$ -component spectrum shows a clear inertial subrange with a spectra slope of  $-5/3$  and a roll-off at high frequencies in the dissipation range. The  $v$  and  $w$  component spectra are almost identical and show less intense velocity fluctuations than the  $u$ -spectra at low frequencies, and larger levels at high frequencies. At the highest frequencies the ratio between the  $v$  or  $w$  spectra and the  $u$  spectra is close to 2, as would be expected of isotropic homogeneous turbulence. Moving in towards the wall the overall level of the  $u$  spectrum rises, but the spectral shape retains the same basic form. The  $v$  and  $w$  spectra, however, change substantially. Most notably the low-frequency levels of the  $w$  spectrum fall at low frequencies as vertical large scale motions are suppressed by the non-penetration at the wall. As the wall is approached this suppression is seen at higher and higher frequencies. However, closest to the wall at  $z/\delta=7\%$ , the  $v$  and  $w$  still show isotropic behavior at the highest frequencies.

## B. Space-time correlations

As discussed in section II, two-point space time correlations were measured in great detail over the thickness of this boundary layer at 30m/s. The two-point grids were established in a 4mm unit of spacing and extended 124-mm from the wall in  $z$  (and to a maximum normal to wall spacing of 120mm) and to a maximum spanwise spacing  $\Delta y$  of 120mm. Of the 31  $z$ -positions defined by this grid 15 of these positions (placed at approximately equal intervals of  $\log(z)$ ) were selected as anchor points. For each anchor point the moving probe was placed at a complete cross section of positions throughout the boundary layer and the 9-component cross spectrum between the fixed and moving probe measured. The cross spectra were assembled into  $12^{\text{th}}$  octave bands and interpolated back on to the full grid. The resulting four-dimensional data set (fixed probe  $z$ , moving probe  $z'$ , spanwise separation  $\Delta y$  and frequency  $\omega$ ) was then organized into a single Matlab array with a structure matching the functional form of the two-point cross spectrum  $G_{ij}(z, z', \Delta y, \omega)$ . This array was then converted to a similar compact form of the two-point correlation function  $R_{ij}(z, z', \Delta y, t)$  by inverse Fourier transform. Care was taken throughout this process to ensure that the final interpolation faithfully represented the original measured data.

One way to show this function is to plot some representative cuts through it. Figure 6(a) shows maps of the 9 components of the correlation for zero spanwise separation and zero time delay  $R_{ij}(z, z', 0, 0)$ . On the diagonal, these maps show the same Reynolds stress profiles seen in figure 4(b), and the dominance of the streamwise normal stress  $u^2$  (seen in  $R_{11}$ ) and the principle shear stress  $uw$  (seen in  $R_{13}$  and  $R_{31}$ ) are clearly seen. Off the diagonal these maps show the magnitude and extent of the normal to wall correlations. We see an anti-correlation between spanwise velocity correlations  $R_{22}$  close to the wall and in the rest of the bottom half of the boundary layer, and a large scale positive correlation between normal-to-wall velocity correlations  $R_{33}$  that extends well beyond the boundary layer edge.

Figure 6(b) shows the zero time delay correlation coefficient as a function of spanwise and normal-to-wall separations from a fixed point at a position 60% of the boundary layer thickness from the wall, i.e.  $R_{ij}(0.6\delta, z', \Delta y, 0)$ . The  $R_{11}$  map shows high correlation in streamwise velocity fluctuations at small spanwise and normal-to-wall separations. Indeed, at zero spanwise separation, correlation in this velocity component exists throughout the majority of the boundary layer. As spanwise separation increases, the correlation slowly decreases until around  $\Delta y/\delta=40\%$  when a sharp drop to zero occurs followed by another gradual decrease to negative correlation. The normal-to-wall velocity correlation  $R_{33}$  behaves similarly to the streamwise velocity correlation but exhibits smaller

overall magnitudes. The spanwise velocity correlations  $R_{22}$  show a different behavior. A positive correlation is observed between  $z/\delta=36\%$  and  $z/\delta=80\%$  for zero spanwise separation and out to  $y/\delta=60\%$  for zero normal-to-wall separation. The  $R_{13}$  and  $R_{31}$  plots show the shear stress correlation. At zero spanwise separation a negative correlation is observed that extends throughout most of boundary layer. As separation in the spanwise direction increases, shear stress correlation decreases to zero around  $y/\delta=30\%$ .

Figure 7 shows two different sets of cuts through the correlation function that reveal something of its behavior in time. Figure 7(a) shows a cut parallel to the wall at 60% of the boundary layer thickness  $R_{ij}(0.6\delta, 0.6\delta, \Delta y, t)$ . Time delay has been multiplied by the free stream velocity and so, through Taylor's hypothesis, the horizontal axis of these maps can be thought of representing streamwise separation, with the downstream direction being to the left. In this view the correlation of the spanwise  $R_{22}$  and wall normal  $R_{33}$  velocity fluctuations are approximately isotropic and extend over 20 to 30% of the boundary layer thickness. These correlations decay monotonically as separation is increased. By contrast, the streamwise velocity correlation  $R_{11}$  is neither monotonic nor isotropic. In the spanwise direction the correlation falls to zero at about half the boundary layer thickness, then falling to a negative minimum at a separation of about  $75\%\delta$ . In the streamwise direction decay of the correlation is much more gradual and significant correlation is seen at separations as large as two boundary layer thicknesses. This elongated flow structure is of aeroacoustic importance since the blades of a rotor system operating in the boundary layer are likely to cut it multiple times, leading to the haystacking phenomenon first seen by Sevik (1970). If we ignore rotor-induced distortion (which would be likely to further elongate the structure), the blades of a 0.46-m diameter scaled version of Sevik's 10-bladed rotor, operated at the design advance ratio of 1.17, would cut the boundary layer at intervals of  $tU_{ref}/\delta=0.53$ .

Figure 7(b) shows correlations of velocity fluctuations with the point at  $z/\delta=60\%$  over a plane perpendicular to the wall, i.e.  $R_{ij}(0.6\delta, z', 0, t)$ . Normal to wall velocity fluctuations  $R_{33}$  are almost isotropic about this point and very similar to those seen in the plane parallel to the wall. Spanwise velocity correlations  $R_{22}$  show a highly directional structure with correlations extending away from and towards the wall on a diagonal ridge that makes an angle of about 30 degrees to the wall (assuming convection at the free stream velocity). There is also a region of negative correlation seen downstream of and beneath the main lobe. Similar directionality is seen in the streamwise velocity correlations, particularly at larger separations. The elongated correlation function visible in the plane parallel to the wall is seen to be a cut through a larger structure extending outward from the wall. Velocity correlations at  $60\%\delta$  show significant correlation with fluctuations in the near wall region three boundary layer thicknesses upstream. One would expect this directionality in the correlations to have a substantial effect on the timing of radial and blade to blade lift correlations seen by a cutting rotor, and thus the radiated sound.

It is important to note that the plots in figures 6 and 7 only represent a tiny fraction of the measured data. For example, using only data at the measured resolution, over 200 plots of the type of figure 7(b) could be drawn, each showing the correlation of velocity fluctuations with a different wall normal location and spanwise separation.

## IV. Sound Predictions

In this section we present predictions for a rotor immersed in a boundary layer that fully accounts for the inhomogeneity and anisotropy of the turbulence and its interaction with the rotor. We use our measurements of the full correlation tensor function to provide the necessary source terms, and the theory of Glegg *et al.* (2012) to relate these to the radiated sound. Predictions are performed for a rotor geometry that closely matches that first used by Sevik (1970). Predictions include spectral content and directivity and are performed for a variety of cases including different rotor immersions and advance ratios.

### A. Rotor Geometry

The rotor geometry used for the sound predictions is illustrated in figure 8. The design is based on a 2.25 scaled version of Sevik's 10-blade rotor that is being fabricated at Virginia Tech for entry into the Virginia Tech Stability Wind Tunnel this fall. The design advance ratio of this rotor is 1.17. The blades have a constant chord of 57.2mm along their span, have no skew, and square tips. The total diameter of the blade plane is 457.2mm, but the hub diameter was increased beyond the 2.25 scaling to 172mm to allow room for instrumentation in the wind tunnel model. The root of each blade was shortened by 6.4mm to account for this adjustment so that the blades have a span of 165.1mm. The blade pitch angle varies nonlinearly along the span from  $55.6^\circ$  at the root to  $21.2^\circ$  at the tip. The airfoil geometry is approximately constant along the span with a maximum thickness of 0.097  $t/c$  at the root and 0.084  $t/c$  at the tip both occurring at mid-chord. The profile and twist of the airfoil section is shown in Figure 8(b).

Future experiments will be conducted to measure the distorted inflow turbulence ingestion of the rotor in the rotating reference frame to compare with prediction. The experimental model includes a long instrumentation



section extending far forward from the leading edge of the blade base 382.8mm. The nose cone is 135.6mm long followed by a 247.1 long 172mm outside diameter tube. This tube will house a wireless DAQ and a 4-channel bridge for a hotwire anemometry system. Select rotor blades will be outfitted with custom miniature X-wire probes so that two-point cross-correlation measurements can be conducted of the inflow 19.1mm ahead of locations along a single blade or between blade pairs. Figure 9 shows the experimental arrangement with the rotor extending out from the wall and the instrumented blades rotating through the boundary layer.

## B. Sound Prediction Methodology

Starting with the Ffowcs Williams Hawkins equation, Glegg *et al.* (2012) develop a theory for the sound radiated by a rotor cutting inhomogeneous turbulence due to unsteady loading. The theory assumes a compact blade chord, and uses a strip theory approach to relate blade upwash fluctuations to unsteady lift. The theory gives the far-field sound pressure spectrum  $S_{pp}$  at observer location  $\mathbf{x}$  and angular frequency  $\omega$  as,

$$S_{pp}(\mathbf{x}, \omega) = \left( \frac{\omega}{c_o r_o} \right)^2 \sum_{n=1}^B \sum_{k=1}^B \sum_{m=-\infty}^{\infty} \int_{R_{hub}}^{R_{tip}} \int_{R_{hub}}^{R_{tip}} K_m(R, \mathbf{x}, \omega) K_m^*(R', \mathbf{x}, \omega) S_{LL}^{(n,k)}(R, R', \omega - m\Omega) e^{-im(\phi_n - \phi_k)} dR dR' \quad (3)$$

where  $\Omega$  is the angular velocity of the rotor and  $c_o$  the speed of sound. The spectrum  $S_{pp}$  depends on a double sum over the blade count  $B$  because it accounts for blade to blade correlations in the unsteady lift. It depends on the double integration with radial distance  $R$  and  $R'$  (on the  $n$ th and  $k$ th blades respectively at angular positions  $\phi_n$  and  $\phi_k$  in the rotor frame) to account for the radial extent of the lift correlation. The Fourier coefficients  $K$  account for the propagation of sound from a blade to the observer and thus also retarded time effects associated with the blade rotation. At radius  $R$  on blade  $n$ , for example, we define

$$-\frac{x_i n_i(R, \tau) e^{i\omega r(\tau)/c_o}}{4\pi r(\tau)} = \sum_{m=-\infty}^{\infty} K_m(R, \mathbf{x}, \omega) e^{-im(\Omega\tau + \phi)} \quad (4)$$

where  $\tau$  represents source time,  $r$  is the instantaneous distance between radius  $R$  and the observer,  $n_i$  are the components of the unit vector in the instantaneous direction of the blade lift, and  $x_i$  are the components of  $\mathbf{x}$ . The unsteady lift cross spectrum between blades  $n$  and  $k$ ,  $S_{LL}^{(n,k)}$ , is determined from the corresponding unsteady upwash spectrum  $S_{ww}^{(n,k)}$  using a straightforward strip-theory application of the two-dimensional Sears function  $S(\sigma)$ , dependent on the reduced frequency based on local chord and blade speed  $\sigma = \omega c / 2U$ ,

$$S_{LL}^{(n,k)}(\omega, R, R') = [\pi \rho_o c U S(\sigma)]_R [\pi \rho_o c U S(\sigma)]_{R'}^* S_{ww}^{(n,k)} \quad (5)$$

Here  $\rho_o$  is the flow density. The upwash cross-spectrum  $S_{ww}^{(n,k)}$  can, in turn, be determined from the two-point space-time correlation of velocity fluctuations in the boundary layer

$$S_{ww}^{(n,k)}(\omega, R, R') = \frac{1}{4\pi^2} \frac{\pi}{T} \int_{-T}^T \int_{-T}^T n_i^{(n)}(R, \tau) n_j^{(k)}(R', \tau') R_{ij}(\mathbf{z}_n(\tau), \mathbf{z}_k(\tau'), \tau - \tau') e^{i\omega(\tau - \tau')} d\tau d\tau' \quad (6)$$

where  $R_{ij}$  is the same two-point space time correlation obtained in the boundary layer measurements, here referenced by the instantaneous position vector of radius  $R$  on blade  $n$  (given by  $\mathbf{z}_n(\tau)$ ) and the instantaneous position vector of radius  $R'$  on blade  $k$  (given by  $\mathbf{z}_k(\tau')$ ). In terms of the coordinates used in describing the measured correlation function,  $\Delta y$  is simply the second component of  $\mathbf{z}_k(\tau') - \mathbf{z}_n(\tau)$ , and  $z$  and  $z'$  are the third components of  $\mathbf{z}_n(\tau)$  and  $\mathbf{z}_n(\tau)$ , respectively.

Note that the above formulation provides sound predictions for a rotor in a free field (i.e. neglecting the reflection plane provided by the wall on which the boundary layer is growing). While including the wall is clearly going to be necessary when we come to predict actual sound levels encountered in the wind tunnel or a practical application, leaving it out as we have done here enables us to examine more directly the spectral form and directivity of the sound field that results from the inhomogeneity and anisotropy of the boundary layer turbulence.

## C. Results

Sound predictions were performed for the Sevik rotor using the above free-field theory and the experimental measurements as input. Boundary layer correlations were measured in sufficient detail to be used explicitly in equation 6, without further empirical input. Predictions were made for free stream velocities of 30m/s and 20m/s. In the latter case the correlation was assumed to scale with the free stream velocity, as justified by the scaling of the Reynolds stresses seen in figure 4(b). Note that the predictions presented here do not attempt to account for any distortion of turbulence generated by the rotor itself. For conditions where the rotor is generating thrust, such distortion would be likely to enhance effects resulting from the turbulence anisotropy.

### 1. Source Terms as Seen in the Blade Reference Frame

Calculations were performed by discretizing two complete rotor rotations into 1024 discrete source time intervals. Blade radius was discretized into 8 values between 58% and 100% of the blade radius. Points inboard of the 58% location were not considered since these would lie outside the edge of the boundary layer for all conditions. The two point space time correlation history  $R_{ij}(\mathbf{z}_n(\tau), \mathbf{z}_k(\tau'), \tau - \tau')$  was then evaluated for each blade pair and combination of radii. Figure 10 shows some examples of the form of this function for  $R=R'=R_{tip}$ . This calculation has been performed for the design rotor advance ratio of 1.17 and a tip clearance of 2cm (8.8% of the blade radius) and the streamwise velocity correlation  $R_{II}$  is shown (this being approximately equal to the upwash). Figure 10(a) shows the correlation for  $n=k$ , i.e. the autocorrelation for velocity fluctuations experienced at one of the blade tips. The origin of the time coordinates is with the blade at top dead center, as far out of the boundary layer as possible. The correlation is plotted against time delays  $\tau$  and  $\tau'$  normalized on free stream velocity and boundary layer thickness. The bottom left to top right diagonal on this figure simply shows the mean square of the turbulent velocity fluctuations experienced by the blade tip as it rotates. The blade cuts through the boundary layer near bottom dead center, at about  $\tau\delta/U_{ref} = 2.7$  and 8, the blade tip spending about  $1/3^{rd}$  of the rotation period immersed in significant turbulence and resulting in repeated islands in the correlation map. Moving off the diagonal we see a decay representing the time delay correlation along the blade tip path. Echoes of the main correlation islands are seen well off the diagonal near  $(\tau'\delta/U_{ref}, \tau\delta/U_{ref}) = (8, 2.7)$  and  $(2.7, 8)$ . These are produced by correlation between the turbulence structure experienced on one blade passage through the turbulence, with structure seen during the next – a direct consequence of the large size of the boundary layer compared to the rotor, and the long streamwise scales of the turbulence.

Figure 10(b) shows results for  $p \equiv n-k = 2$ , i.e. the cross correlation of velocity fluctuations at one blade tip and the blade tip of the second following blade. Note that for a rotor with evenly spaced identical blades the absolute indices of the blades is of no consequence and only the difference in blade indices denoted here as  $p$ , is important. This, incidentally, implies that the double sum over blade indices in equation (1) can be replaced by a single summation over  $p$ , significantly reducing the computational effort required in making a sound prediction. For  $p=2$  the main correlation islands shift to the right by a time equivalent to  $1/5^{th}$  of a full rotation for this 10-bladed rotor. This simply represents the time delay between the leading and trailing blades cutting the same turbulence structures. Correlation magnitudes in the two principal islands are somewhat lower than in figure 10(a) because of the natural decay of the turbulence that takes place over this interval. As the correlation map shifts to the right the upper left echo, representing the correlation from blade  $k$  to the second passing of blade  $n$ , strengthens since the time delay is now only  $4/5$ ths of a rotation. At the same time the bottom right echo (representing  $6/5$ ths of a rotation from blade  $n$  to the second pass of blade  $k$ ) weakens and drops below the lowest contour level. Correlation maps for other blade spacings appear similar with the rightward shift increasing as the blade separation counter  $p$  is increased, and the left hand echoes growing to replace the original correlation islands on the diagonal once  $p$  reaches the blade count  $B$ .

Figures 11 through 13 show examples of the blade upwash cross-spectrum  $S_{ww}^{(n,k)}(\omega, R, R')$  plotted in terms of coherence. These have been calculated according to equation (6) and again we have taken the streamwise velocity fluctuations as representative of the blade upwash. Figure 11 shows coherence between different radial locations and the blade tip on the same blade. The organization of the boundary layer turbulence is clearly visible in the high coherence values seen over the outer 20% of the blade radius, a length roughly equivalent to half the boundary layer thickness. The coherence peaks at a non-dimensional frequency  $\omega\delta/U_{ref} \approx 10$ . In order to infer the corresponding spatial scale we take the timescale corresponding to this frequency and multiply by the blade tip speed. This calculation gives a distance of about 1.7 boundary layer thicknesses, a number that can be explained in terms of the correlation maps of figure 7(a). Specifically we see here the streamwise velocity correlation having a negative lobe for spanwise separations between  $0.6$  and  $0.9\delta$ . As the blade traverses this correlation function in the spanwise

direction it will see a dominant large scale structure with a wavelength of between 1.2 and 1.8 boundary layer thicknesses.

Blade to blade coherence between velocity fluctuations seen at the tip are shown in figure 12. The maximum coherence (again seen at around  $\omega\delta U_{ref} \approx 10$ ) is about 0.5 between adjacent blades ( $p=1$ ), and falls to about 0.2 for  $p = 2$ . Coherence values are all less than 0.1 for larger blade separations up to  $p = 5$ . For  $p = 6, 7, 8$  and  $9$  coherence traces exactly match those for  $p = 4, 3, 2$  and  $1$ , respectively. This is simply a consequence of the rotational symmetry of the blades, the relationships between velocity fluctuations at the tips of blades  $1$  and  $2$ , being identical to that between blades  $10$  and  $1$ , for example.

Blade to blade coherence between velocity fluctuations seen at the blade tip and at the 95% and 90% radial locations on following blades are shown in figure 13. Here we see the development of an interesting and important asymmetry. Looking first at the 95% radius (figure 13(a)), we see for  $p=1$  lower coherence values than for  $p=9$ . A similar difference is seen comparing  $p=2$  and  $8$ ,  $3$  and  $7$ . This asymmetry results from the inclination of the boundary layer structures, relative to the wall, seen in the spanwise and streamwise velocity component correlations of figure 7(b). Such structures produce a correlation between velocity fluctuations in the upper part of the boundary layer and fluctuations seen at a later time close to the wall. Thus, a rotor cutting the turbulence will thus see stronger coherence between velocity fluctuations at an inboard point on one blade and at the tip of a following blade ( $p = 9, 8, 7$ ) than in the reverse situation ( $p = 1, 2, 3$ ). Figure 13(b) shows that this asymmetry is actually greater at larger radial separations even though the coherence itself is smaller.

## 2. Noise results

The actual upwash cross spectrum was calculated by taking into account the change in blade angle along the radius of each blade as well as the complete four dimensional space time correlation function meaning the velocity fluctuations in all three directions are considered. Blade radii were discretized into 10 logarithmically spaced locations starting at the blade tip and decreasing to 60% of the blade radius since outside of this area the rotor blades do not produce significant sound. Source time intervals were computed exactly as discussed in the previous section. After calculating the actual unsteady upwash spectrum, the far-field sound spectrum  $S_{pp}$  was evaluated as a function of observer location  $\mathbf{x}$  by utilizing equations (3-6). All noise predictions are compared to a baseline case where design conditions consist of a free stream velocity of 20m/s, boundary layer thickness of .102m, advance ratio of 1.17 to match Sevik, and gap of 20.3mm between the wall and blade tips.

By restricting the observer to a location 5 meters directly downstream on the axis of the rotor the effect of various operating and flow conditions can be analyzed. Figure 14 shows sound predictions for various advance ratios ( $J$ ) with all other conditions remaining the same. An increase in advance ratio with free stream velocity remaining constant effectively means a decrease in rotor rpm. This decrease in rotor rpm decreases the blade passing frequency thus causing the haystacking humps to occur at lower frequencies. Also, an increase in advance ratio means blade to blade correlation in the boundary layer decreases causing the overall decibel levels to drop by about 11 dB from an advance ratio of 0.7 to 1.44. An advance ratio of 1.44 represents the rotor's zero thrust condition, as predicted by JavaProp, meaning there would be no distortion present in the inflow. For  $J=0.7$  the haystacking phenomenon in the sound spectrum is noticeable over 6 blade passing frequencies compared to only 4 for an advance ratio of 1.44. Since we are not accounting for distortion in the present noise predictions, results are most realistic for the  $J=1.44$  case, but likely underestimate the haystacking for  $J=1.17$  and  $0.7$ .

The amount the rotor is immersed in the boundary layer also plays a significant role in sound production. Figure 15 shows a comparison between 3 different rotor immersions designated by the distance the tip of the rotor blades get to the wall. The red line represents the baseline condition of a tip gap of 20.3mm. As shown in the figure, increasing the tip gap by a factor of 2 from the baseline condition to 40.6mm decreases the sound spectrum over the entire frequency range by about 5 dB without changing the spectral shape. This is expected since an increase in the gap between the wall and rotor blade means less blade immersion and interaction with turbulence. Decreasing the gap to 10.15mm increases the sound level at blade passing frequencies only slightly by approximately 0.3 dB. This is due to the fact that the majority of the turbulence in the boundary layer was already interacting with the rotor blades when there was a tip gap of 20.3mm. Figure 16 shows the comparison between the design condition of  $U_\infty=20\text{m/s}$  and  $U_\infty=30\text{m/s}$ . As expected the increase in free stream velocity increases both the sound spectrum across the frequency range and shifts the haystacking effect to higher frequencies. The shift in frequency of the haystacks occurs because in order to increase the free stream velocity and remain at the design advance ratio of 1.17, the rotor angular velocity must be increased. The reason for the increase in dB can be seen in equation (5). The Sears function  $S(\sigma)$  is proportional to  $U_\infty$  making the unsteady lift proportional to  $U_\infty^4$ . This means increasing  $U_\infty$  from 20 to 30m/s increases the total dB by  $10\log_{10}(30^4/20^4)$  or approximately 7 dB which is shown in Figure 16.

To determine the directivity of the sound produced by the rotor the sound pressure was evaluated at various locations in the far-field all a distance of 5 meters from the center of the rotor. Analysis about the spanwise axis can be seen in Figure 17 where 0 degrees represents an observer located directly downstream of the rotor and 90 degrees represents the location in the plane of the rotor on the normal to wall axis. Figure 17(a) shows the directivity for various advance ratios evaluated at the first blade passing frequency for each case. All three cases show the rotor sound field deviates from a simple streamwise dipole and acts more like a monopole as advance ratio decreases. At an advance ratio of 0.7 the sound pressure at 90 degrees is 51 dB which is about 11dB less than the sound pressure level in the streamwise direction. Increasing the advance ratio to 1.44 causes a noticeably larger difference in the sound pressure level at 90 degrees and 0 degrees. This effect is consistent with most of the noise being produced by the blade tips. The directivity is also slightly asymmetric about the streamwise axis presumably because of the asymmetry of the source in the boundary layer. Figure 17(b) shows the behavior of the rotor at the baseline condition at its first 3 blade passing frequencies. The difference in sound levels between an observer at 90 degrees and 0 degrees decreases from the first BPF to the third BPF meaning the rotor radiates sound more like a dipole at higher frequencies. Figure 18(a) shows the directivity at the first blade passing frequency for various advance ratios about the normal to wall axis. An angle of 0 degrees again represents an observer location directly downstream on the axis of the rotor and an angle of 90 degrees represents the location in the plane of the rotor along the spanwise axis. The same effect of deviation from a simple streamwise dipole is also present although absolute sound levels differ. The sound level at  $\pm 90^\circ$  about the normal to wall axis is about 0.5 dB higher than at  $\pm 90^\circ$  about the spanwise axis. Analysis of the baseline condition for the first three blade passing frequencies can be seen in Figure 18(b). The directivity about the normal to wall axis exhibits the same behavior as Figure 17(b) where the rotor acts more like a dipole at higher frequencies.

## V. Conclusions

The present study is concerned with the aerodynamics and aeroacoustics of a rotor partially immersed in a thick turbulent boundary layer. This simple configuration recreates in a canonical setting the important physics produced when a rotor ingests inhomogeneous anisotropic turbulence, without many of the complications present in most practical applications. In this paper we present detailed measurements of turbulence structure the inflow boundary layer that are used to completely evaluate the source terms for rotor noise predictions using the theory of Glegg *et al.* (2012). The boundary layer was generated in the anechoic test section of the Virginia Tech Stability Wind Tunnel. 3-component hot-wire measurements showed the boundary layer to be closely two-dimensional, have a thickness of 101mm and a momentum thickness Reynolds number of 16,600 at a free stream speed of 30m/s. To provide the source terms needed to predict the sound produced by a rotor immersed in this boundary layer it is necessary to document the complete space time correlation tensor function of the boundary layer in the cross-flow plane. This four dimensional function was obtained with a resolution of 4% of the boundary layer thickness by measuring the two-point cross-spectrum tensor between two 4-sensor hot wire probes traversed to over 1800 different relative positions in the boundary layer. When reconfigured into a useable form these measurements provide a detailed view of the boundary layer turbulence. In particular, the measurements show large scale correlation structure elongated in the streamwise direction and inclined at about 30 degrees to the wall. This elongated structure is associated with negative correlations of the streamwise velocity at larger spanwise separations and has an overall spanwise scale (negative lobe to negative lobe) of about 1.5 boundary layer thicknesses.

The boundary layer data, and the Glegg *et al.* theory were used to perform sound predictions for a 0.457-m diameter rotor partially immersed in the boundary layer. This rotor (which is currently being fabricated for future wind tunnel tests) has 10 unskewed constant chord blades and is a 2.25-scale version of that used by Sevik (1970). The theory requires the evaluation of the correlation and cross spectrum of upwash velocity fluctuations seen in the frame of reference of the rotor blades. This was evaluated directly from the experimental measurements. Blade radial and blade to blade crossspectra show the strongest coherence at a non-dimensional frequency that corresponds closely to the cross-flow scale of the boundary layer turbulence divided by the blade tip speed. Blade to blade coherence estimates also show substantial asymmetry produced by inclination of the dominant boundary layer structure relative to the wall.

Free-field sound predictions were performed as a function of advance ratio, rotor immersions (measured in terms of tip gap) and free stream speed. No attempt was made to include the effect of the wall on the sound propagation since we were interested in revealing directly the effects of the non-uniformity of the turbulence sound directivity. At all conditions sound spectra were found to be broadband, but show ‘haystacks’ - rounded peaks at multiples of the blade passing frequency produced when blades cut the same correlated patch of turbulence multiple times. Overall sound levels were found to strongly depend on the flow and operating conditions shown by a difference of 11 dB over the range of advance ratios analyzed. In real life we would expect the haystacking at lower advance ratios to be enhanced by the stretching of the turbulence as it is drawn into the rotor – an effect neglected in the present calculations.

Directivity measurements showed the rotor sound field to deviate noticeably from a simple streamwise dipole. Decreasing advance ratio enhanced this effect making the rotor radiate sound more like a monopole consistent with the sound generated being dominated by the blade tips.

### Acknowledgements

The authors would like to thank the Office of Naval Research, in particular Drs. Ki-Han Kim and John Muench, under grant N00014-10-1-0908. We would also like to acknowledge Dr. Bill Blake for his helpful suggestions and insight and Messrs. Jon Forest, Manuj Awasthi and Tim Meyers for their assistance with the tunnel test.

### References

1. Atassi H and Logue M, 2009, “Fan broadband noise in isotropic turbulence”, AIAA paper 2009-3148.
2. Awasthi M., Forest J., Morton M., and Devenport W., 2011 “The Disturbance of a High Reynolds Number Turbulent Boundary Layer by Small Forward Steps”, AIAA-2011-2777, 17th AIAA/CEAS Aeroacoustics Conference, Portland, Oregon, June 5-8.
3. Blake, W., Mechanics of Flow Induced Sound and Vibration, Wiley, New York, 1986
4. De la Rosa Blanco E, Hall C and Crichton D, 2007, “Challenges in the Silent Aircraft Design”, AIAA paper 2007-454.
5. Glegg S, Morton M and Devenport W, 2001, “Rotor Noise Caused by a Boundary Layer: Noise Predictions”, 18<sup>th</sup> AIAA/CEAS Aeroacoustics Conference, June 4-6, Colorado Springs CO.
6. Devenport W, Burdisso R, Borgoltz A, Ravetta P and Barone M, 2010, “Aerodynamic and Acoustic Corrections for a Kevlar Walled Anechoic Wind Tunnel”, AIAA 16th AIAA/CEAS Aeroacoustics Conference, June 7th-9th 2010, Stockholm, Sweden. AIAA Paper 2010-3749.
7. Devenport W J, Wenger C W, Glegg S A L and Miranda J A, 1998, "Wavenumber frequency spectra in a lifting wake for broadband noise prediction", AIAA Journal, vol. 36, no. 6, pp. 881-887.
8. Forest J B and Devenport W, 2011, “The Wall Pressure Spectrum of High Reynolds Number Rough-Wall Turbulent Boundary Layers”, 17th AIAA/CEAS Aeroacoustics Conference, June 6th-8th, Portland OR, AIAA-2011-2741
9. Ganz U, Joppa P, Patten T and Sharpf D, 1998, “Boeing 18-inch fan rig broadband noise test”, NASA/CR-1998-208704.
10. Gavin. J. R and Lauchle. G. C. 2000. Modelling the timespace correlations in the wake region of a turbulent boundary layer. Proc of ASME winter meeting, Orlando, Florida.
11. Glegg S and Walker N, 1999, “Fan noise from blades moving through boundary layer turbulence”, AIAA paper 1999-1888.
12. S Glegg, M Morton, W Devenport, 2012, “Rotor Inflow Noise Caused By a Boundary Layer: Noise Predictions”, AIAA 18<sup>th</sup> AIAA/CEAS Aeroacoustics Conference, June 4<sup>th</sup>-6<sup>th</sup> 2012, Colorado Springs CO.
13. Graham, J. M. R., “The Effect of a Two-Dimensional Cascade of Thin Streamwise Plates on Homogeneous Turbulence,” Journal of Fluid Mechanics, Vol. 356, 1998, pp. 125–147.

14. Grace S, Atassi H and Blake W, 1996, "Inverse aeroacoustic problem for a streamlined body. Part 1: Basic formulation", *AIAA Journal*, vol. 34, pp. 2233-2240.
15. Grace S, Atassi H and Blake W, 1996, "Inverse aeroacoustic problem for a streamlined body. Part 1: Accuracy of Solutions", *AIAA Journal*, vol. 34, pp. 2241-2246.
16. Hanson D, 1974, "Spectrum of rotor noise caused by atmospheric turbulence", *Journal of the Acoustical Society of America*, vol. 56, pp. 110-126.
17. Hileman J I, Spakowsky Z S, Drela M and Sargeant M A, "Airframe design for silent aircraft", *AIAA paper* 2007-453.
18. Joseph P and Parry A, 2001, "Rotor/wall boundary layer interaction broadband noise in turbofan engines", *AIAA paper* 2001-2244.
19. Huyer S and Beal D, 2007, "A turbulent inflow model based on velocity modulation", *Journal of Sound and Vibration*, vol. 308, pp. 28-43.
20. Huyer S and Snarski S, 2003, "Analysis of a turbulent propeller inflow", *Journal of Fluids Engineering*, vol. 125, pp. 533-542.
21. Ko A, Schetz J and Mason W, "Assessment of the Potential Advantages of Distributed-Propulsion for Aircraft", *ISABE-2003-1094*, XVI International Symposium on Air Breathing Engines (ISABE), Cleveland, Sep 2003.
22. Kota V and Wright M, 2006, "Wake generator control of inlet flow to cancel flow distortion noise", *Journal of Sound and Vibration*, vol. 295, pp. 94-113.
23. Lynch D, Blake W and Mueller T, 2005, "Turbulence correlation length-scale relationships for the prediction of aeroacoustic response", *AIAA Journal*, vol. 43, pp. 1187-1197.
24. Lynch D, Blake W and Mueller T, 2005, "Turbulent flow downstream of a propeller, Part 1: Wake turbulence", *AIAA Journal*, vol. 43, pp. 1198-1210.
25. Lynch D, Blake W and Mueller T, 2005, "Turbulent flow downstream of a propeller, Part 2: Ingested propeller-modified turbulence", *AIAA Journal*, vol. 43, pp. 1211-1220.
26. Majumder S and Peake N, 1998, "Nose generation by the interaction between ingested turbulence and a rotating fan", *Journal of Fluid Mechanics*, vol. 359, pp. 181-216.
27. Martinez R, 1997, "Broadband sources of structure-borne noise for propulsors in "haystacked" turbulence", *Computers and Structures*, vol. 65, pp. 475-490.
28. Minniti R, Blake W and Mueller T, 2001, "Inferring propeller inflow and radiation from near-field response, Part 1: Analytic development", *AIAA Journal*, vol. 39, pp. 1030-1036.
29. Minniti R, Blake W and Mueller T, 2001, "Inferring propeller inflow and radiation from near-field response, Part 2: Empirical application", *AIAA Journal*, vol. 39, pp. 1037-1046.
30. Moiseev N, Lakshminarayana B and Thompson D, 1978, "Noise due to interaction of boundary layer turbulence with a compressor rotor", *Journal of Aircraft*, vol. 15, pp. 53-61.
31. Moser, R. D., Kim, J., and Mansour, N. N., "Direct Numerical Simulation of a Turbulent Channel Flow up to  $Re\tau=590$ ", *Physics of Fluids*, Vol. 11, No. 4, April 1999, pp. 943-945.
32. Muench J, 2001, "Periodic acoustic radiation from a low aspect ratio propeller", PhD dissertation, University of Rhode Island.
33. Mugridge B D, "Axial flow fan noise caused by inlet distortion", *Journal of Sound and Vibration*, vol. 40, pp. 497-512.
34. Plas A P, Madami V, Sargeant M, Greitzer E, Hall C, Hynes T, "Performance of a Boundary Layer Ingesting Propulsion System", *AIAA Paper* 2007-0450, 2007
35. De la Rosa Blanco E, Hall C A, Crichton D, 2007, "Challenges in the Silent Aircraft Engine Design", 45<sup>th</sup> AIAA Aerospace Sciences Meeting and Exhibit, Jan 8-11, Reno NV, AIAA-2007-0454

36. Sevik, M., "Sound Radiation from a Subsonic Rotor Subjected to Turbulence," Symposium on Fluid Mechanics, Acoustics and Design of Turbomachinery, August 31 to September 3, 1970, The Pennsylvania State University, NASA SP 304.
37. Sharpf D and Mueller T, 1995, "An experimental investigation of the sources of propeller noise due to the ingestion of turbulence at low speeds", *Experiments in Fluids*, vol 18, pp. 277-287.
38. Stephens D and Morris C, 2009, "Sound generation by a rotor interacting with a casing turbulent boundary layer", *AIAA Journal*, vol. 47, pp. 2698-2708.
39. Subramanian S and Mueller T, 1995, "An experimental study of propeller noise due to cyclic inflow distortion", *Journal of Sound and Vibration*, vol. 183, pp. 907-923.
40. Wittmer K S, Devenport W J and Zsoldos J S, 1998, "A Four Sensor Hot Wire Probe System for Three Component Velocity Measurements", *Experiments in Fluids*, vol. 24, pp 416-423. See also vol. 27, no. 4, pp. U1, September 1999.
41. Wojno J, Mueller T and Blake W, 2002, "Turbulence ingestion noise, Part 1: Experimental characterization of grid-generated turbulence", *AIAA Journal*, vol. 40, pp. 16-25.
42. Wojno J, Mueller T and Blake W, 2002, "Turbulence ingestion noise, Part 2: Rotor aeroacoustic response to grid generated turbulence", *AIAA Journal*, vol. 40, pp. 26-32.

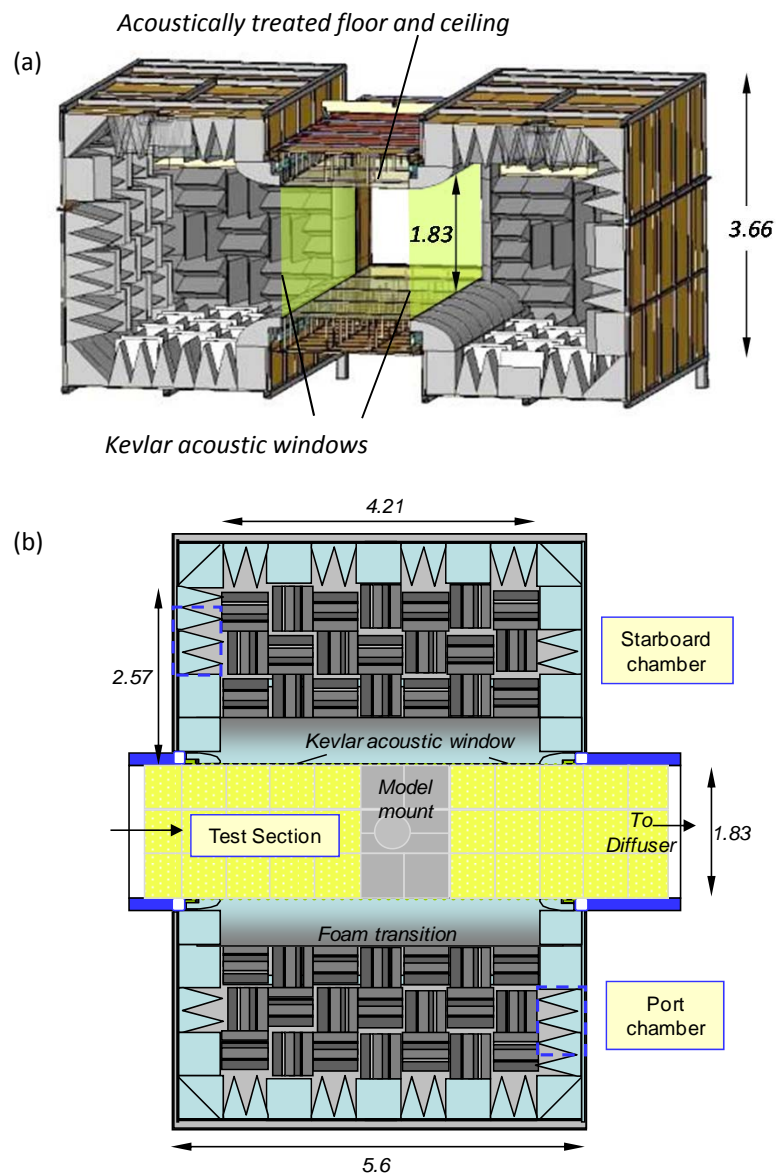


**Figure 1.** Virginia Tech Stability Tunnel Anechoic test section with adjoining anechoic chambers. All dimensions in meters. (a) Perspective view of a cross section perpendicular to the flow path. (b) Plan view schematic.



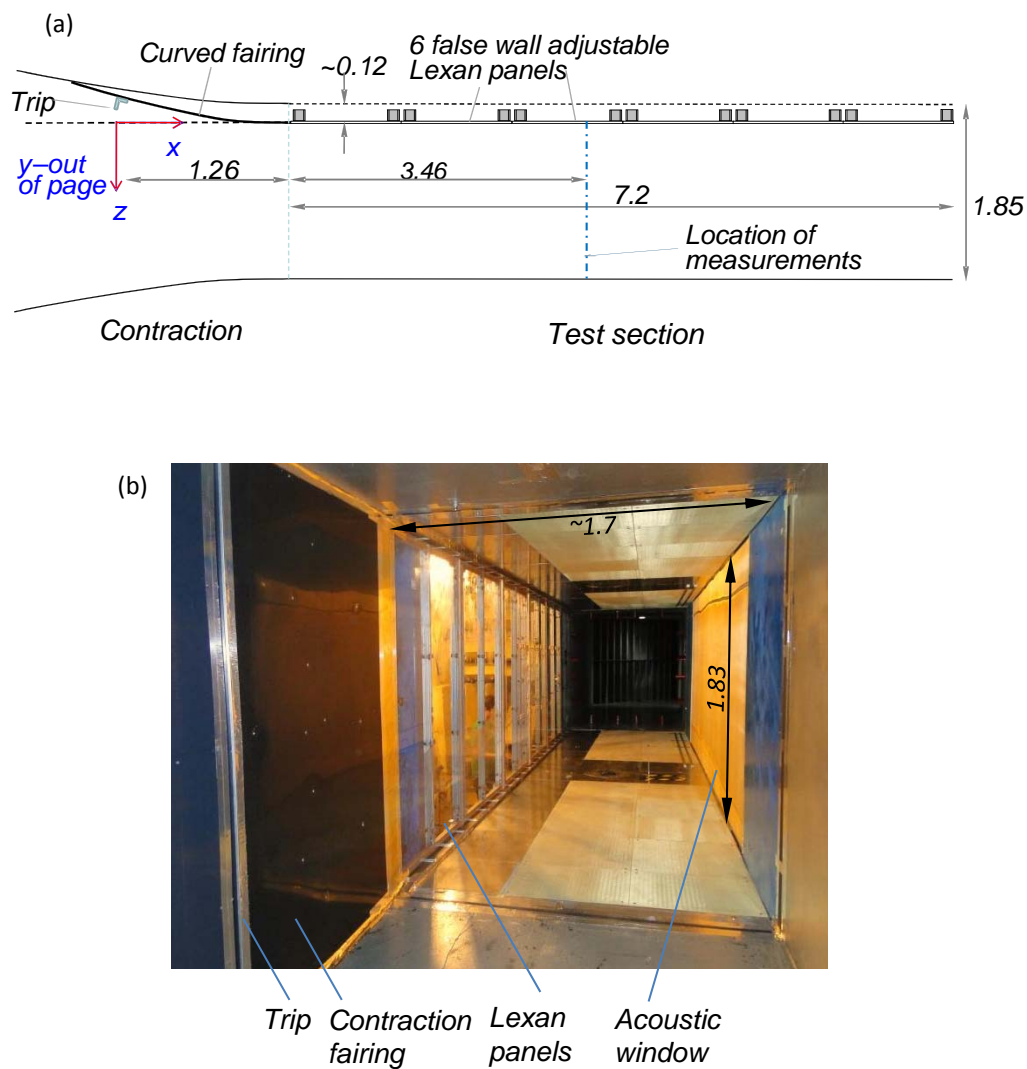


**Figure 2.** Test section in hemi-anechoic configuration. Dimensions in meters. (a) Plan view cross section. (b) Photograph taken from upstream.

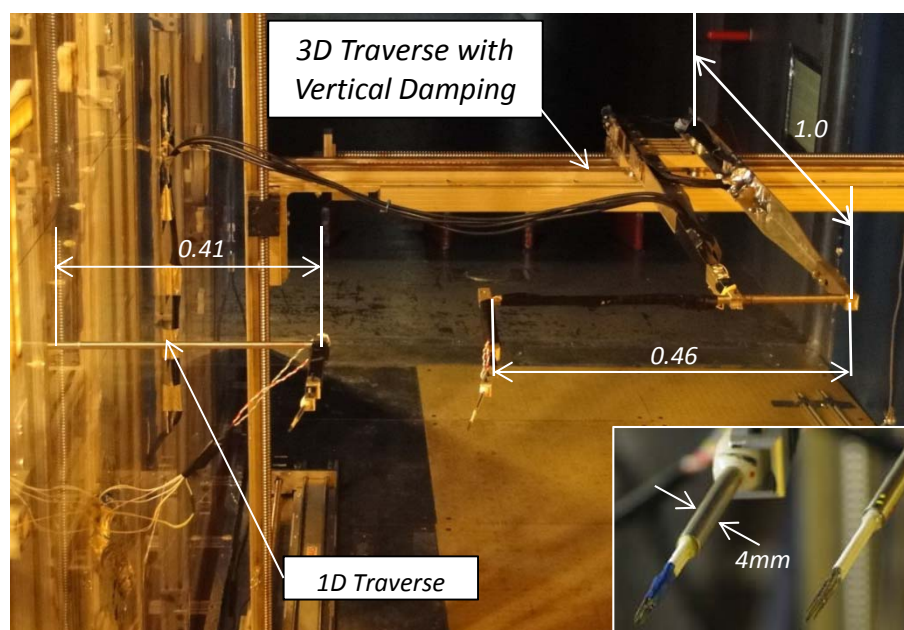


**Figure 3.** Three axis and single axis traverse with probes mounted. Inset shows detail of the probe tips.  
Unmarked dimensions in meters

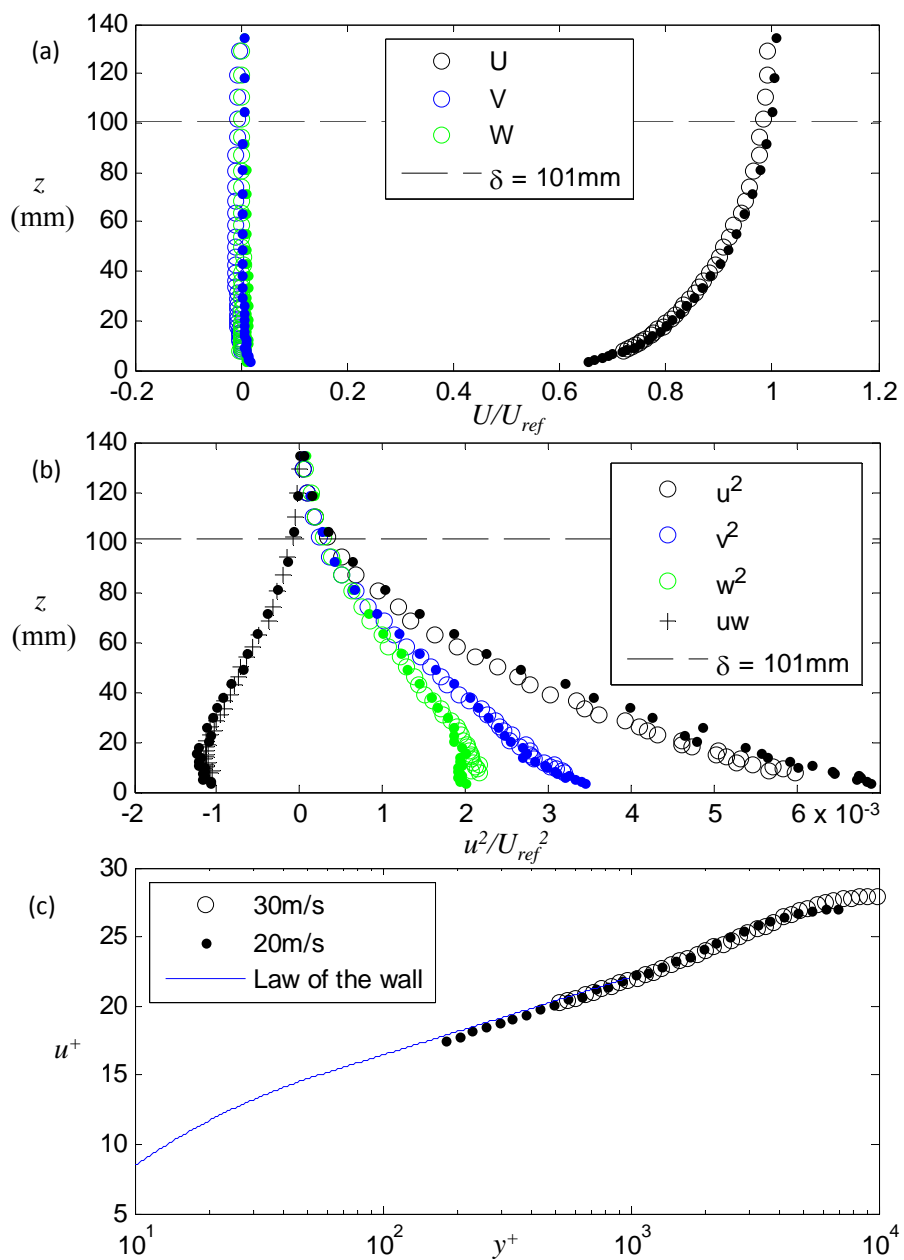


**Figure 4.** Single-point mean velocities and turbulence profiles at 30m/s (circles) and 20m/s (dots). (a) Mean velocities, as a fraction of the free-stream velocity. (b) Turbulence stresses, normalized on free stream velocity. (c) Streamwise mean velocity profiles in wall coordinates.

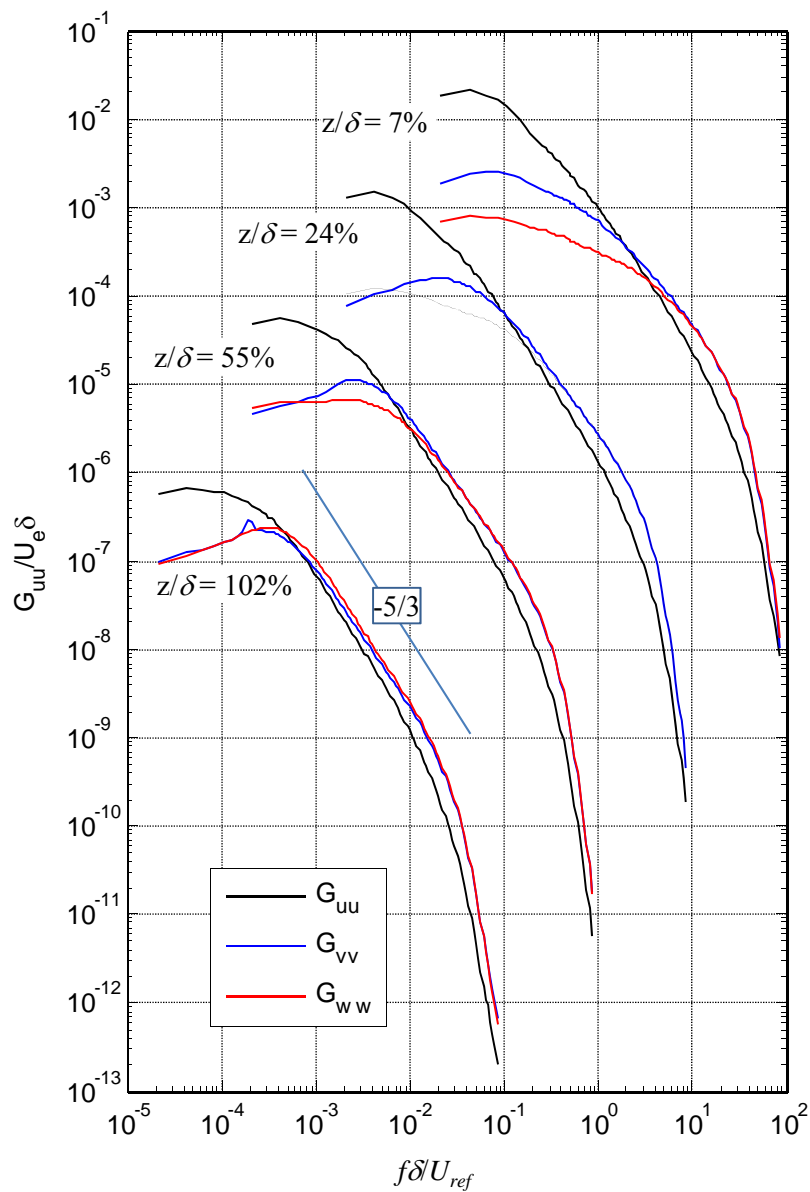


**Figure 5.** Autospectra of velocity fluctuations measured at various positions within the boundary layer. Spectral levels and frequencies are multiplied by 0.1, 0.01 and 0.001 for  $z/\delta=24\%$ ,  $55\%$  and  $102\%$ , respectively.

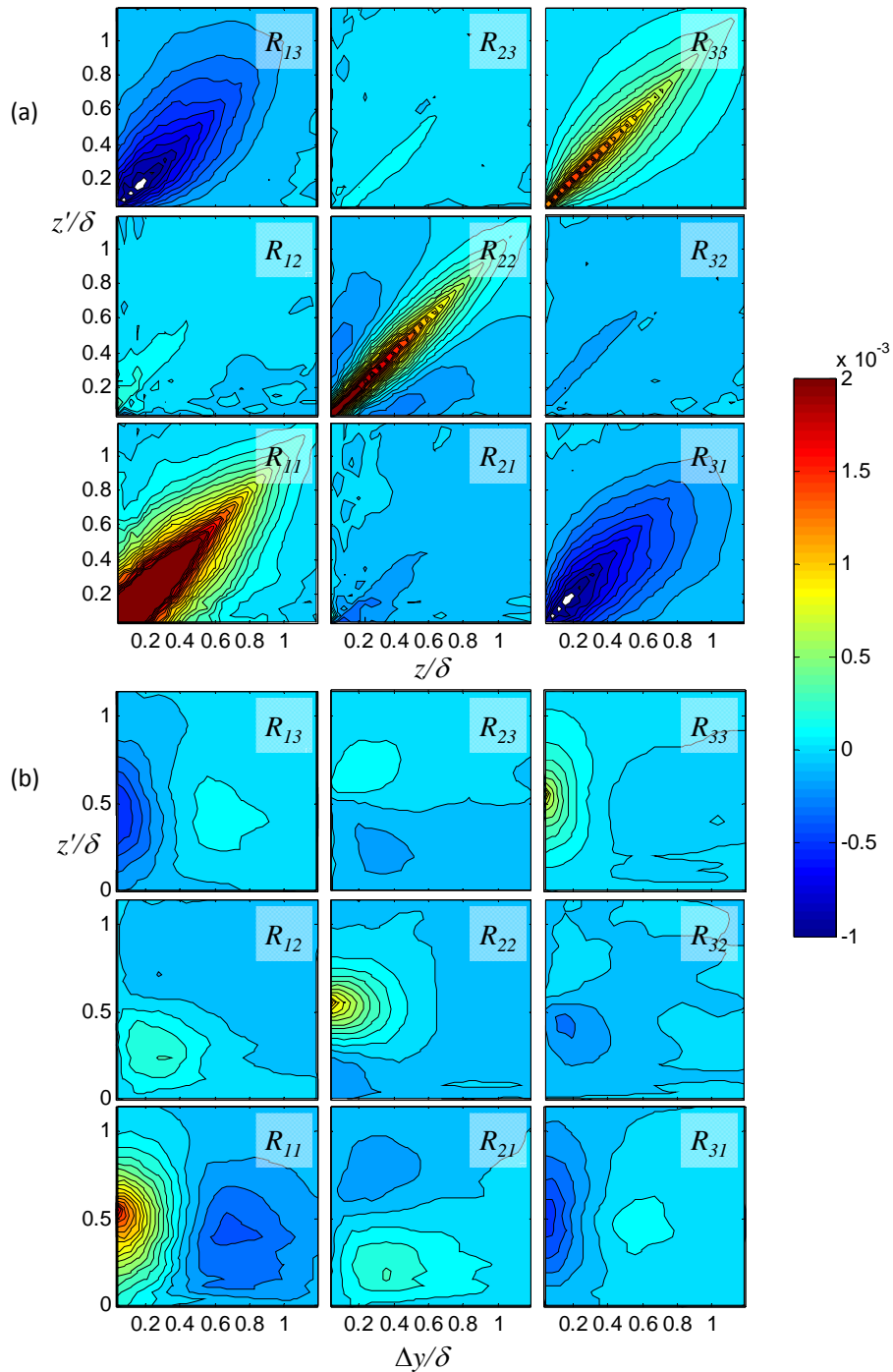


**Figure 6.** Cuts through the four dimensional two-point cross correlation function for all 9 components, normalized on free stream velocity. (a)  $R_{ij}(z, z', 0, 0)$ . (b)  $R_{ij}(0.6\delta, z', \Delta y, 0)$

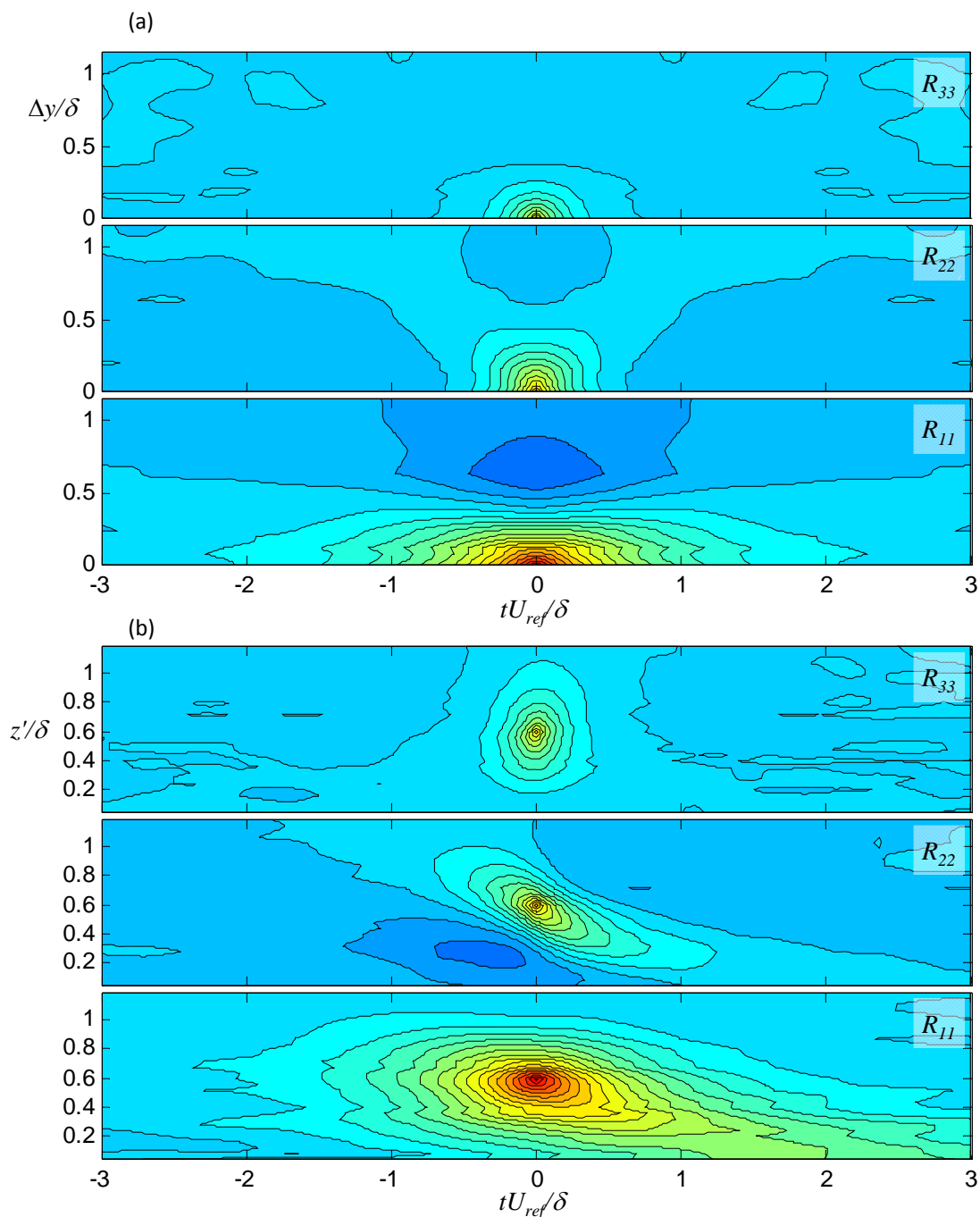


**Figure 7.** Cuts through the four dimensional two-point cross correlation function for the 3 normal components, normalized on free stream velocity. Contour levels same as in figure 6. (a)  $R_{ij}(0.6\delta, 0.6\delta, \Delta y, t)$ . (b)  $R_{ij}(0.6\delta, z', 0, t)$

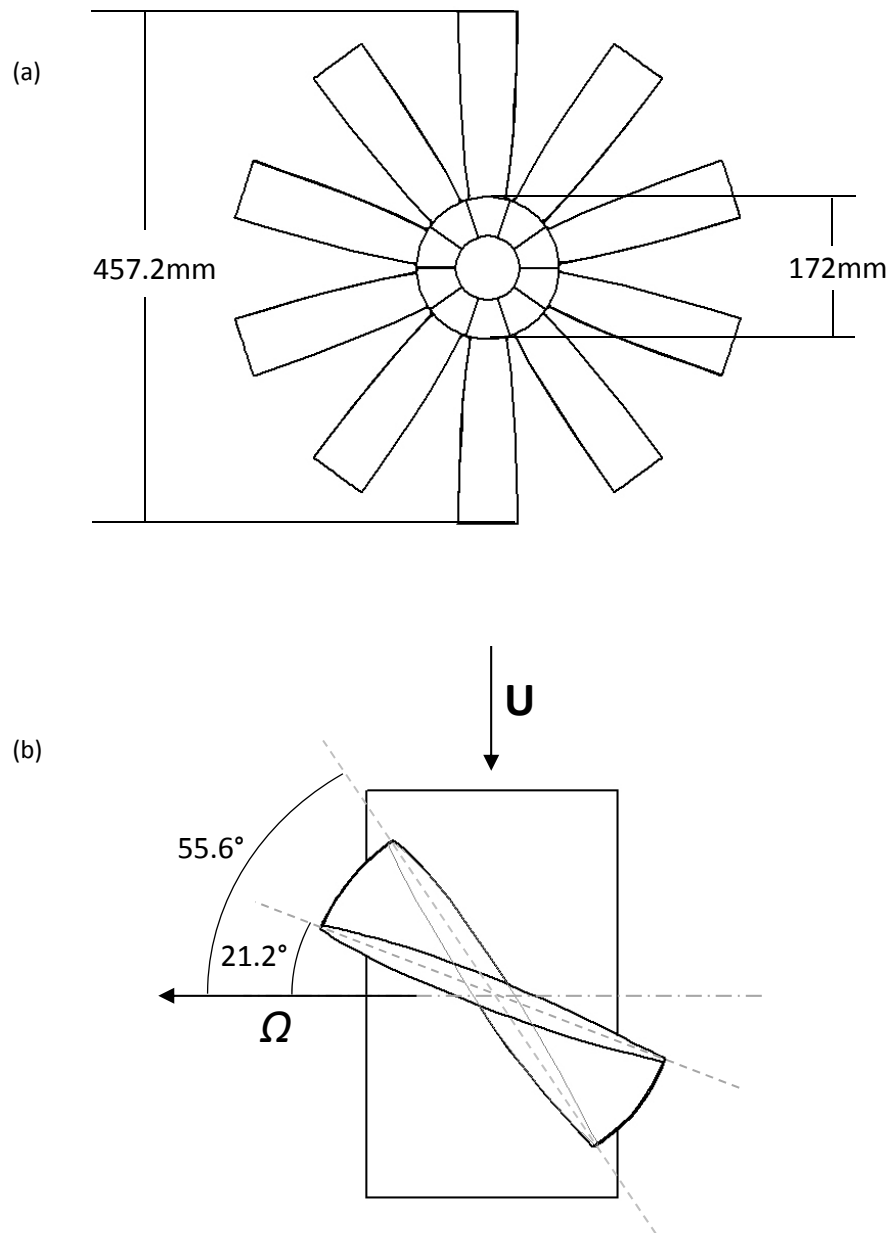


**Figure 8.** Rotor diagram and single blade diagram of twist

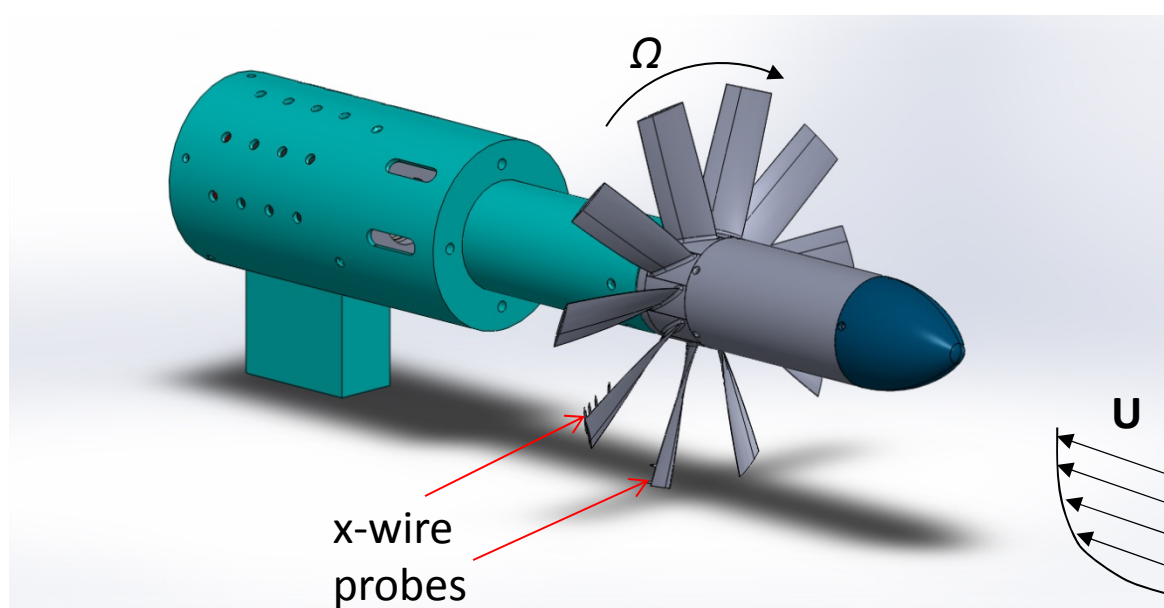


**Figure 9.** Experimental arrangement for rotor-frame two-point cross-correlation measurements Aerodynamic fairings for motor housing and support strut not shown



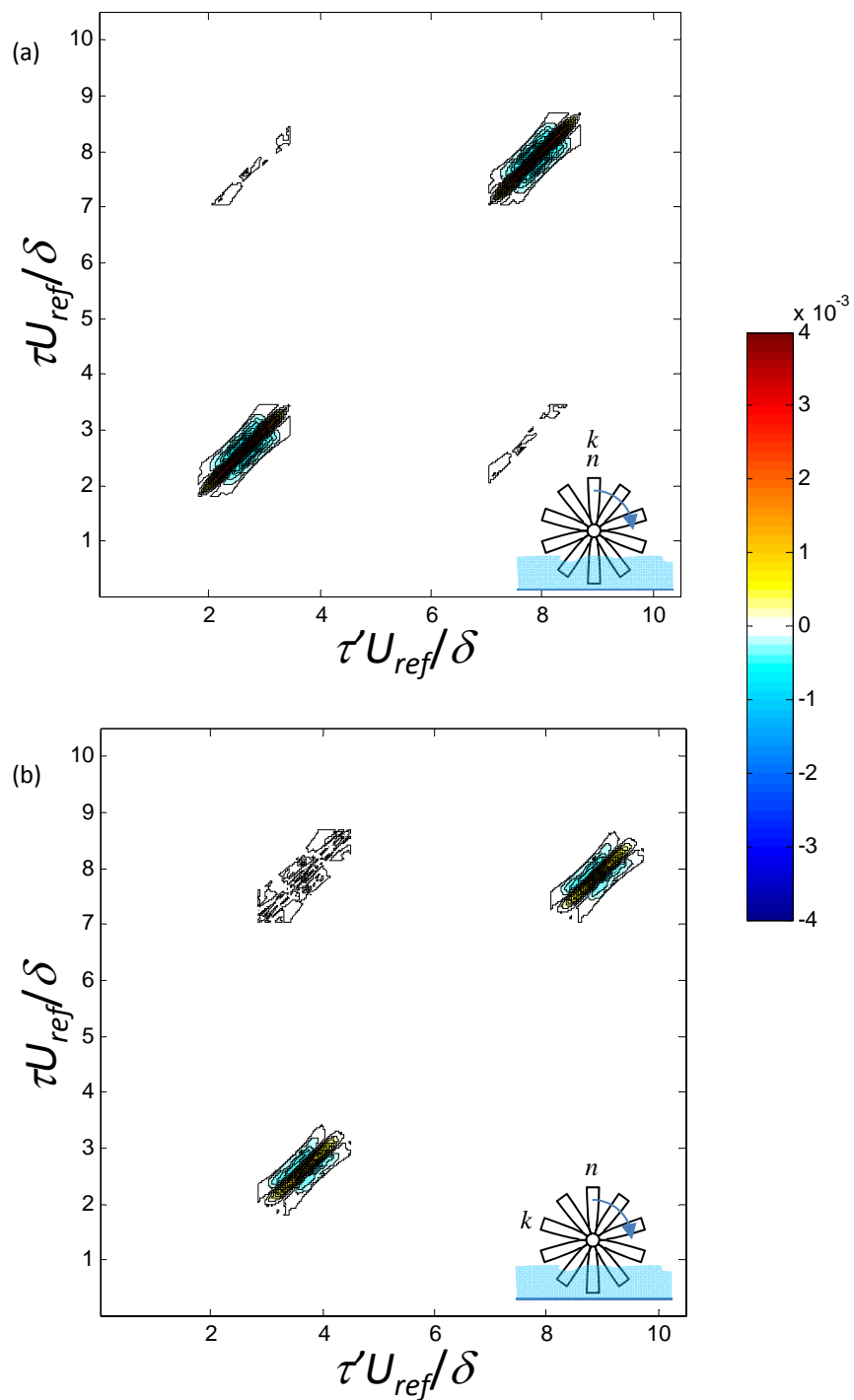


**Figure 10.** Streamwise velocity correlations seen at the blade tips, normalized on free stream velocity. (a) Autocorrelation for  $n=k$ . (b) Cross correlation for  $n-k=2$ .

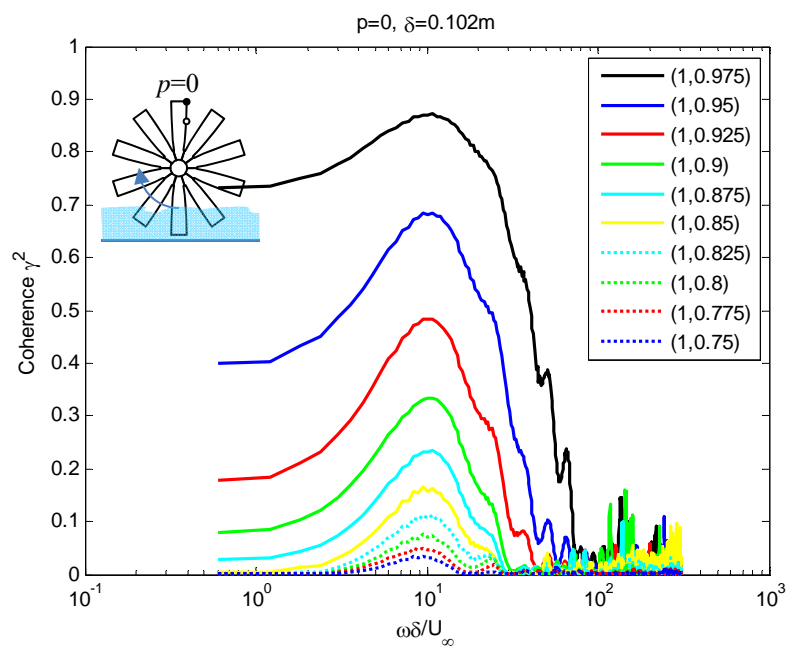


**Figure 11.** Spanwise coherence between streamwise velocity fluctuations seen on the same blade. Correlations are between the blade tip (filled circle on inset) and an inboard position (open circle). Proportionate radial positions for these locations are given by the two numbers listed in each legend entry.

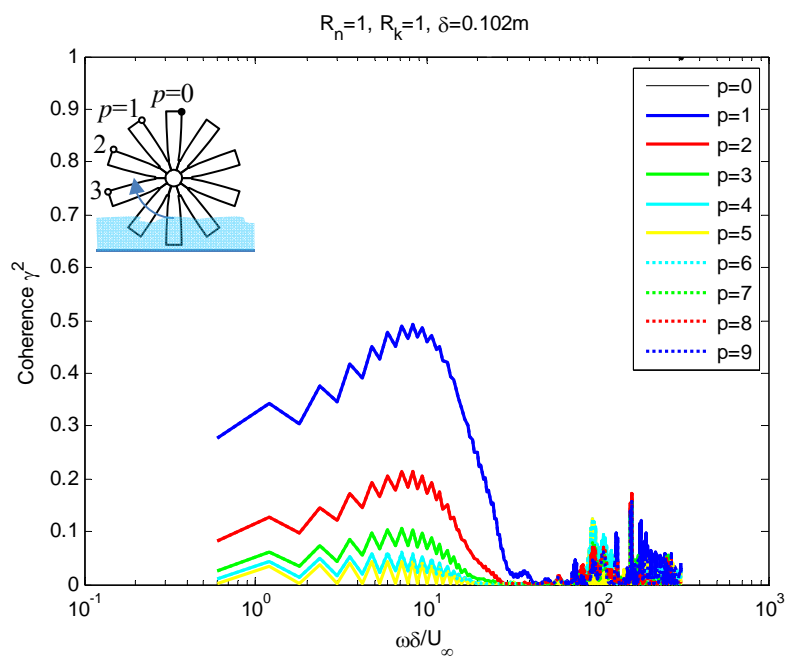


**Figure 12.** Blade to blade coherence of streamwise velocity fluctuations seen at the blade tip. Coherence traces are shown for different blade number differences  $p$ . Note that traces for  $p=6, 7, 8$  and  $9$ , exactly overlay traces for  $p=4, 3, 2$  and  $1$ , respectively.

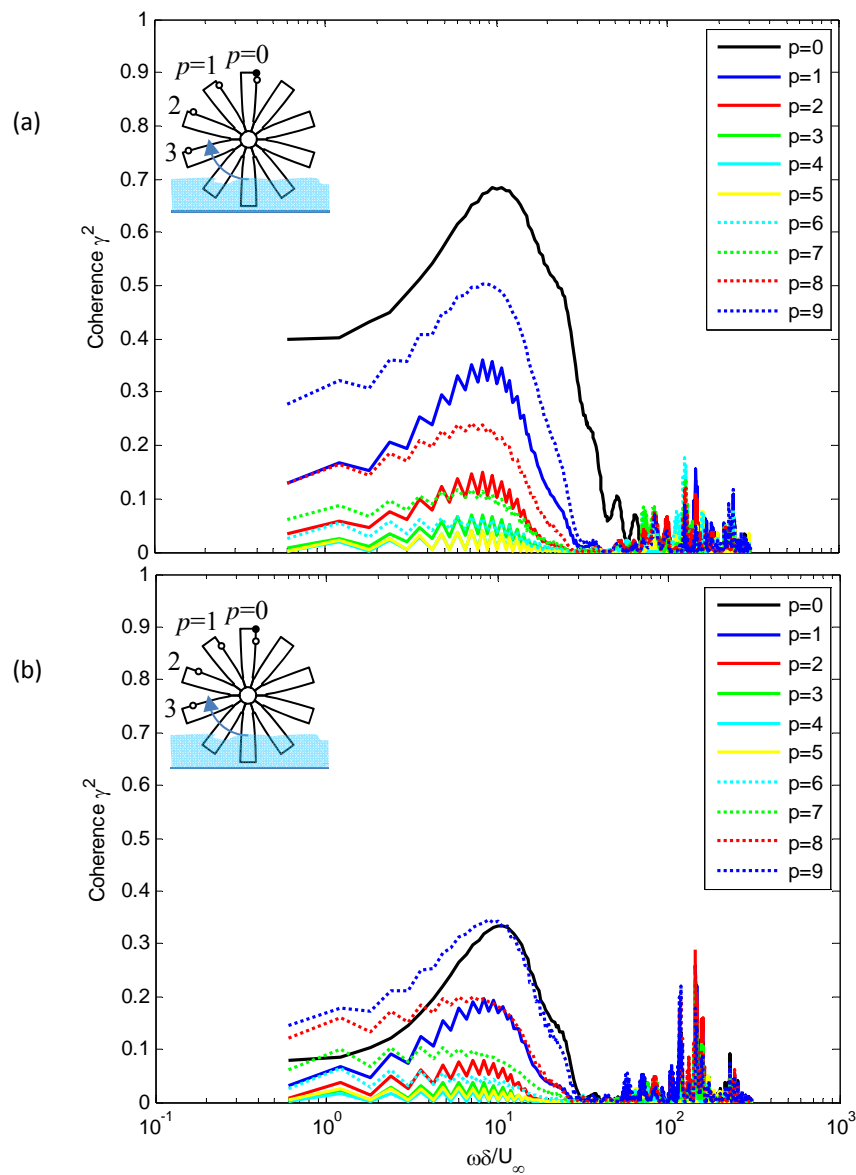


**Figure 13.** Blade to blade coherence between streamwise velocity fluctuations seen at the blade tip and at the (a) 95% and (b) 90% radial locations on following blades. Coherence traces are shown for different blade number differences  $p$ . Note that traces for  $p = 6, 7, 8$  and  $9$ , now lie above traces for  $p = 4, 3, 2$  and  $1$ , respectively.

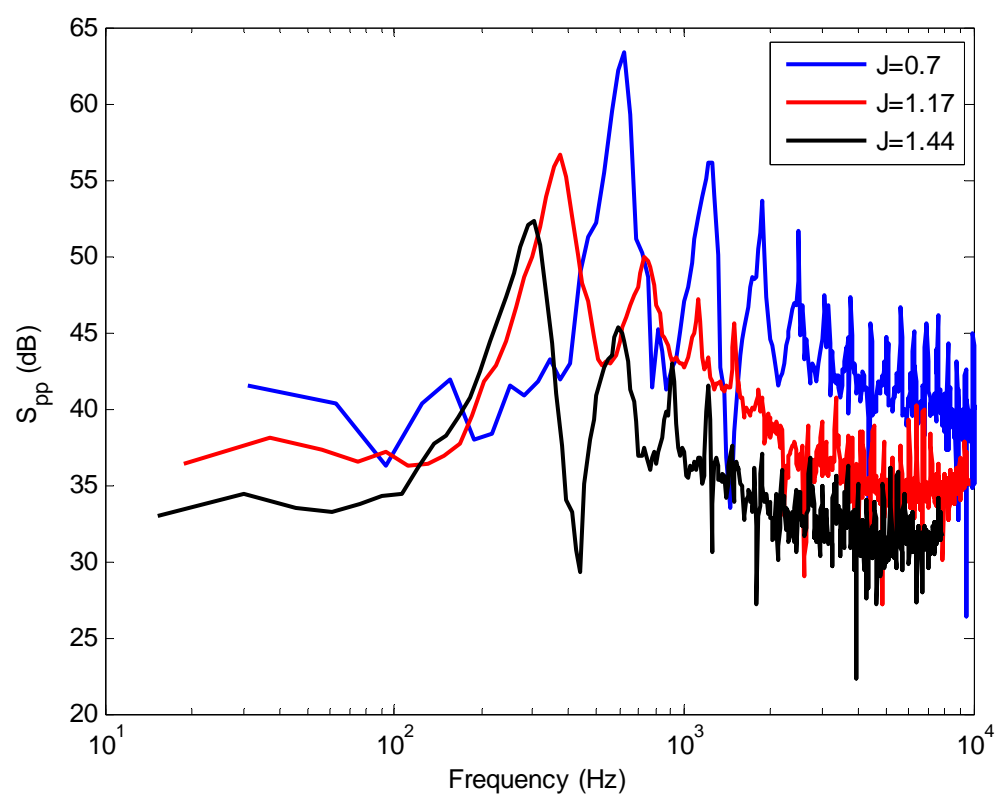


**Figure 14.** Sound spectrum predictions at advance ratios of 0.7, 1.17 (design), and 1.44 (zero thrust).

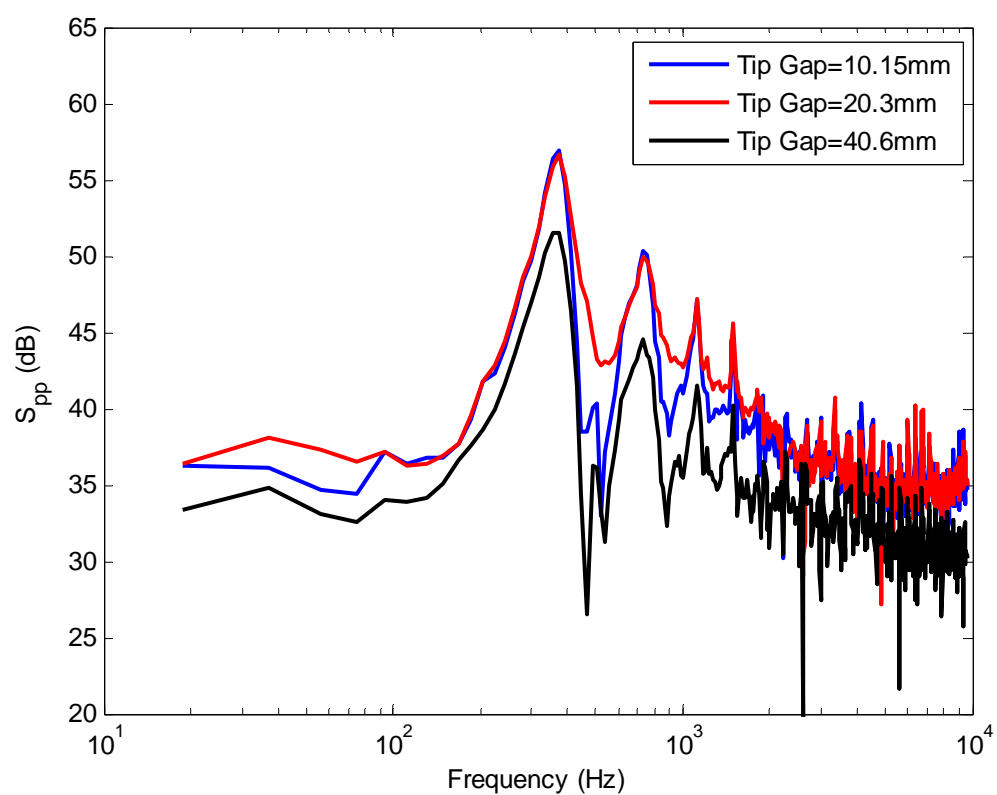


**Figure 15.** Sound spectrum predictions for various rotor immersion depths.

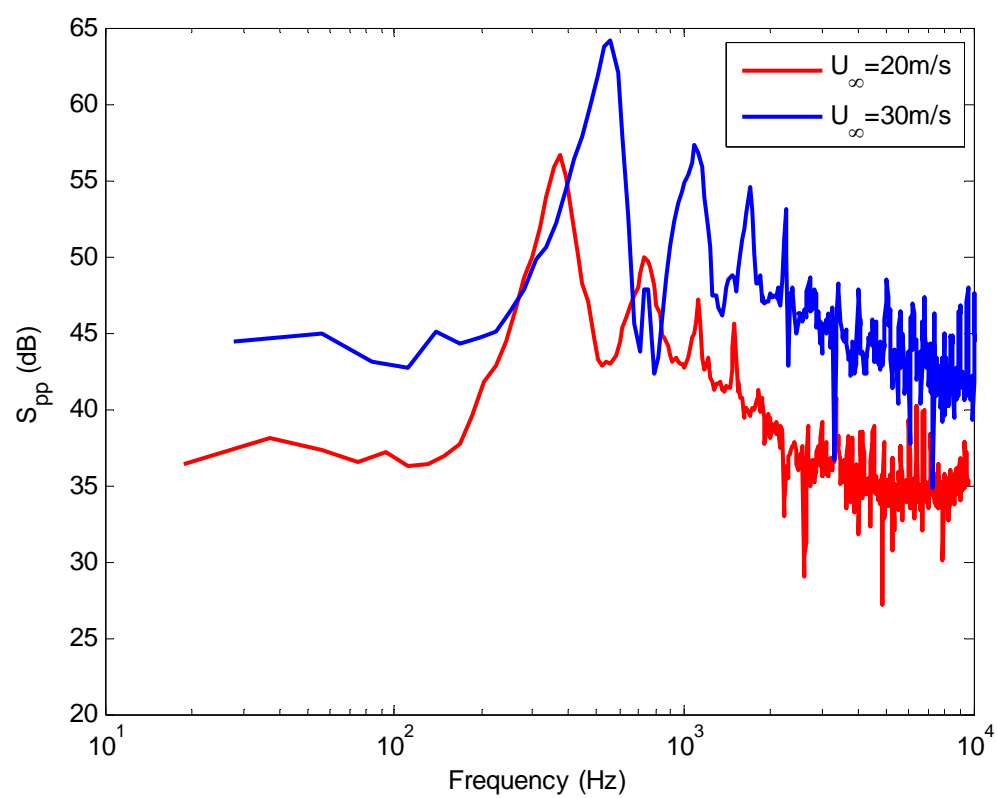


**Figure 16.** Comparison of sound levels predicted at the design velocity of 20m/s and 30m/s.

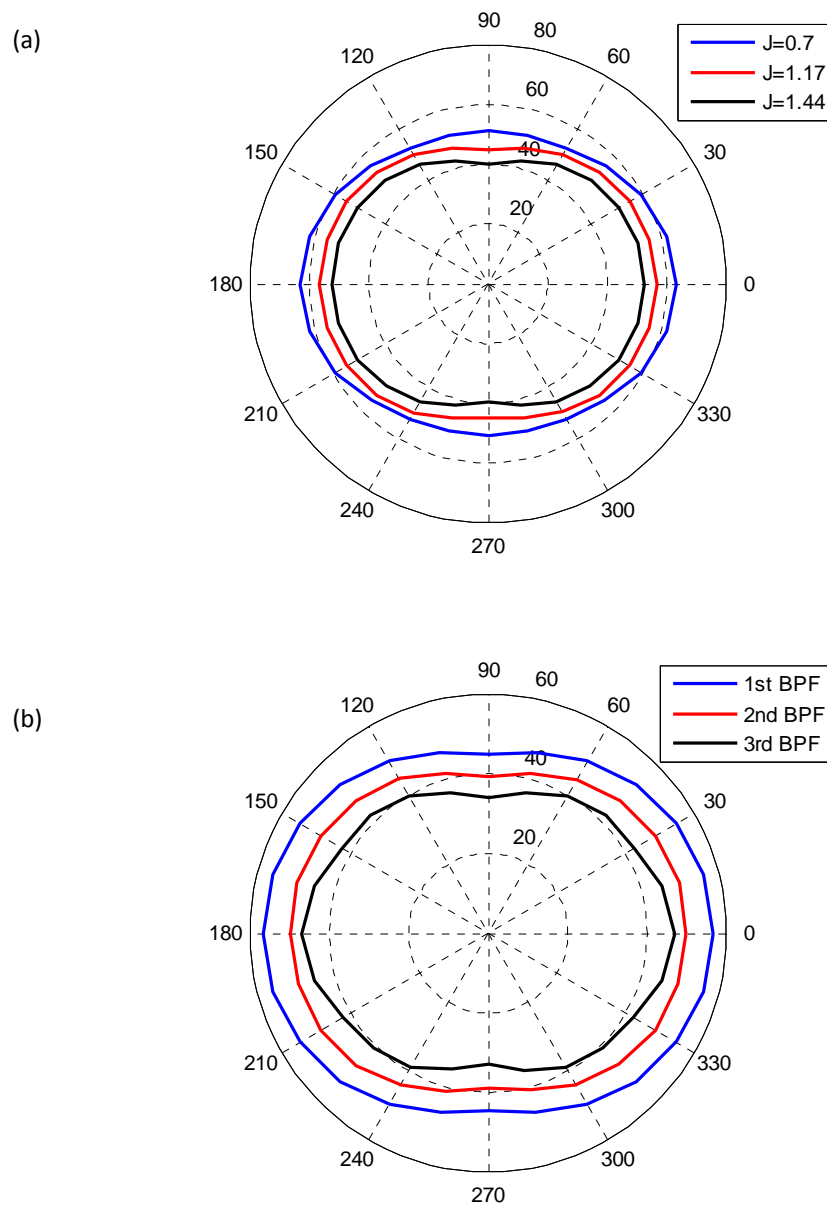


**Figure 17.** Directivity plots about the spanwise axis of (a) various advance ratios and (b) the first three blade passing frequencies of the baseline condition of  $J=1.17$ . Levels are in dB



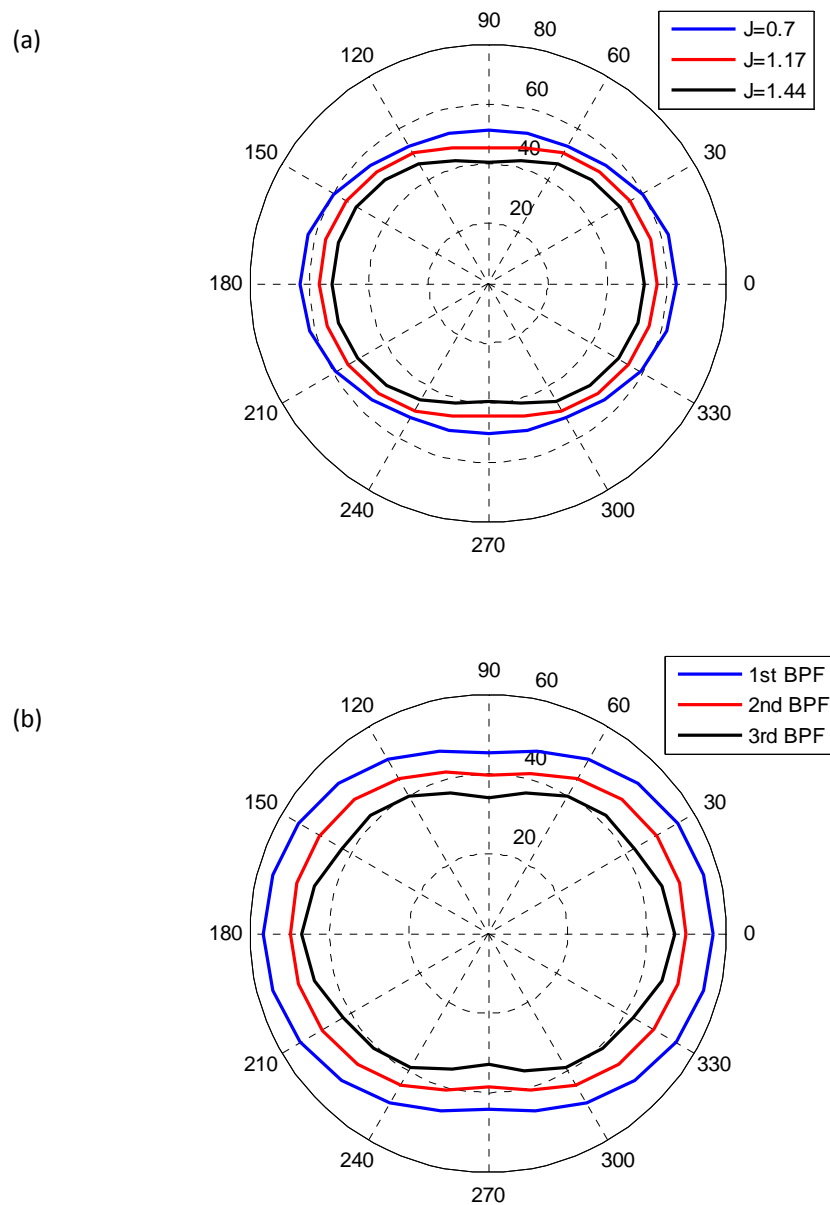


**Figure 18.** Directivity plots about the normal to wall axis of (a) various advance ratios and (b) the first three blade passing frequencies of the baseline condition of  $J=1.17$ . Levels are in dB.